ARTICLE | Article in Press

Seismic performance and hybrid retrofit strategies for a historical four-legged masonry minaret

Adnan Kiral · Zeliha Tonyali · Mustafa Ergun · Muhammet Yurdakul · Ali Ekber Sever · Pınar Usta Evci

Received: 25 June 2026 / Accepted: 29 September 2026
© The Author(s) 2026

Abstract

Comparisons of global response modification and local strengthening for a complex heritage monument remain limited. This study evaluates lead-rubber-bearing (LRB) and friction-pendulum-bearing (FPB) isolation, carbon-fibre-reinforced polymer (CFRP) fabric and laminate, steel plates, and their hybrid combinations for the historical Four-Legged Minaret in Diyarbakır, Türkiye. A three-dimensional equivalent-continuum layered-shell macro-model was subjected to nonlinear direct-integration time-history analysis using one DD-2/ZD spectrum-compatible ground motion. The unretrofitted structure developed tensile-stress concentrations at the lower column–beam–body and upper balcony–shaft transitions. After isolation, corresponding maximum tensile stresses were 2.741 and 4.375 MPa for LRB and 0.813 and 4.740 MPa for FPB, showing that isolation alone did not control every critical local demand. Under the idealised full-bond assumption, all representative hybrid configurations satisfied the project-specific 2 MPa design-control target in both strengthened and adjacent regions; their all-region maxima ranged from 1.194 to 1.685 MPa for LRB and from 1.142 to 1.231 MPa for FPB. Steel plates gave the lowest demands inside the applied bands, but stress redistribution sometimes shifted the all-region maximum into adjacent masonry. The findings are scenario-specific and do not demonstrate crack prevention or unconditional safety; multi-record, site-specific and interface-validated assessment is required before implementation.

Keywords Historical four-legged masonry minaret · Seismic retrofitting · Base isolation · CFRP strengthening · Steel-plate strengthening · Nonlinear time-history analysis

Introduction

Historical masonry minarets are among the most seismically vulnerable structures because of their high aspect ratios and slender, cantilevered geometries[1,2]. Although these structures are iconic elements of cultural heritage, their architectural configuration—typically comprising a massive base, a transition segment and a slender shaft—presents significant structural challenges[3]. Their dynamic sensitivity is associated with a high centre of gravity and low natural frequencies, which can promote resonance when seismic excitation approaches the fundamental

This Article in Press is shared early to give you faster access to new research. It is citable and carries a permanent DOI. The final edited version will replace it automatically.

https://doi.org/10.1038/s41598-026-74380-z

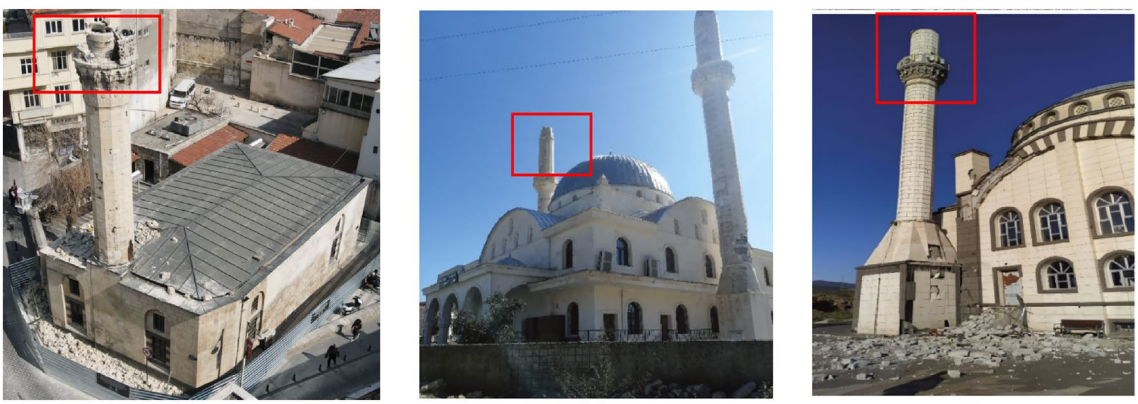
Published online: 10 October 2026

scientific reports

period[4–6]. The geometric discontinuity between the rigid base and flexible shaft acts as a critical stress raiser and may lead to localised failure[7,8]. Combined with the low tensile capacity of traditional masonry, seismic actions may induce severe bending demand, horizontal cracking and overturning instability[9–11]. The wider 2023 Kahramanmaraş earthquake damage context and minaret-specific field observations are documented in[12,13]; representative minaret damage patterns are presented in Fig. 1. These observations emphasise the need for detailed seismic assessment and compatible retrofit strategies. Recent studies have therefore examined the seismic performance and vulnerability of historical masonry mosques and minarets[14–16].

Seismic retrofitting of historical masonry structures requires carefully balanced interventions that enhance structural performance while preserving cultural and architectural integrity. Within this framework, strengthening methods are generally classified as local interventions or global response-modification strategies. Fibre-reinforced polymer (FRP) composites have received considerable attention because of their high strength-to-weight ratio, corrosion resistance and limited visual impact on heritage fabric[17,18]. Experimental and numerical studies have demonstrated their capacity to improve the strength and deformation capacity of masonry elements[19,20]. For minarets, stepwise FRP strengthening has been shown to redistribute damage away from critical regions and improve seismic capacity[21]. The number of FRP layers required to achieve a prescribed stiffness may, however, increase installation time and cost. Carbon-fibre-reinforced polymer (CFRP) can provide comparatively high axial stiffness with fewer layers, although its effectiveness remains strongly dependent on the bond between the composite and the masonry substrate; debonding and local stress concentrations remain important limitations[21–24]. In contrast, base isolation modifies the global dynamic response by reducing the seismic demand transmitted to the masonry superstructure[25–30]. A hybrid strategy combining lead-rubber bearings (LRBs) with supplemental viscous dampers (VDs) has also been reported to reduce displacement, drift and stress demands in a historical minaret[31]. Alternative vibration-control strategies have included liquid-column dampers, for which reductions in displacement and stress demand have been reported under earthquake excitation[32]. Case-specific local strengthening has likewise been shown to improve stiffness and reduce displacement demand in damaged minarets[33].

Despite the growing literature on historical masonry assessment, systematic comparisons of global response-modification and local strengthening strategies for a single geometrically complex monument remain limited. The historical Four-Legged Minaret was therefore evaluated using a common numerical model and a common spectrum-compatible seismic input. The investigated alternatives comprised lead-rubber-bearing (LRB) and single-friction-pendulum-bearing (FPB) isolation, carbon-fibre-reinforced-polymer (CFRP) fabric, CFRP laminate, steel-plate strengthening and their hybrid combinations. The investigation was structured as a controlled deterministic comparison rather than as a probabilistic or code-compliance assessment. Its contribution lies in the



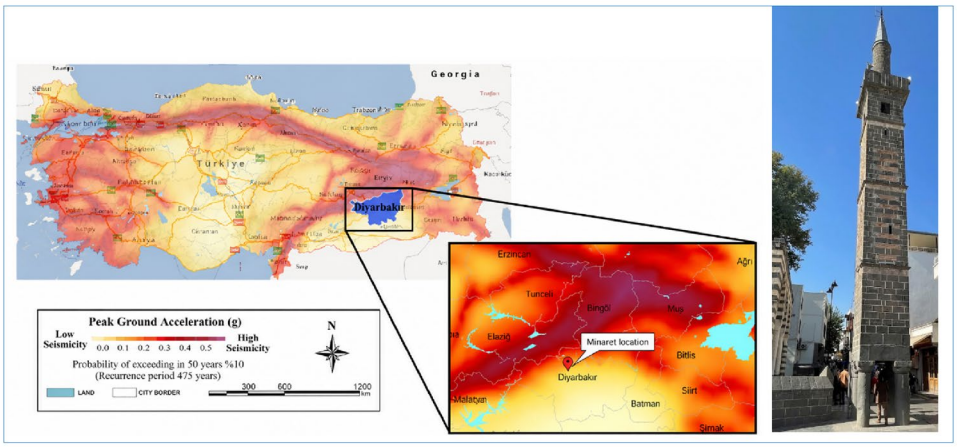
(a) (b) (c)

Fig. 1 Representative post-earthquake damage to minarets after the 2023 Kahramanmaraş earthquake sequence: (**a**) image taken by author; (**b**) and (**c**) modified after Ref.[13].

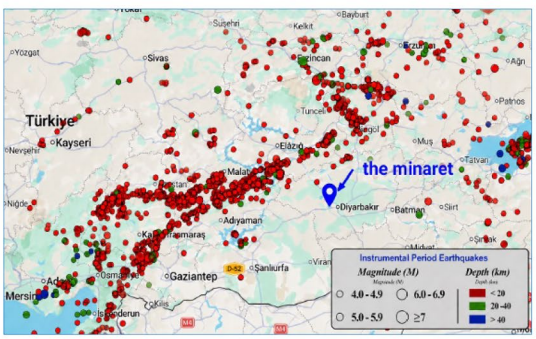
mechanics-based comparison of retrofit categories under identical modelling and loading assumptions, together with an explicit evaluation of conservation criteria and model limitations. Record-to-record dispersion and statistical ranking stability are reserved for a dedicated multi-record extension of the framework.

Description of the minaret

The Four-Legged Minaret is one of the most distinctive historical masonry structures in Diyarbakır, Türkiye (Fig. 2)[34,35]. It belongs to the Şeyh Mutahhar Mosque, located in the Sur district, within the historical urban fabric of the city. According to the inscription on the mosque, the minaret was constructed in 906 Hijri, corresponding to approximately 1500 AD, during the Akkoyunlu period under Sultan Kasım. Unlike conventional Ottoman or Anatolian minarets, the structure is not directly supported by a continuous base or massive pedestal; instead, its upper body rests on four independent slender basalt columns, which gives the monument its unique architectural and structural identity. In addition, the minaret is currently located close to a road exposed to vehicle-induced vibrations. Urban development around the mosque has reduced the original courtyard area, leaving the minaret more exposed to traffic-induced dynamic effects. These factors may have contributed to long-term damage accumulation, differential settlement, and crack development in the lower structural system. The Four-Legged Minaret was also affected by the 6 February 2023 Kahramanmaraş earthquakes. Post-earthquake assessments reported the extension of pre-existing cracks and the formation of new joint separations, particularly around the monolithic beam and transition zone above the four supporting columns. Numerical investigations performed in



(a)



(b)

Fig. 2. (**a**) Location of the Four-Legged Minaret and (**b**) historical seismicity of the surrounding region. The maps were obtained from the AFAD online map (see Ref.[37]) and adapted for this figure. The photograph of the minaret was taken by the authors.

a previous study[36] showed that the highest stress concentrations occur in this same region, confirming that the column–beam–body transition is the most vulnerable part of the structure under seismic excitation.

The minaret consists of three main structural parts: the lower four-column support system, the main masonry body, and the upper balcony–shaft region. The lower support system is composed of four independent cylindrical basalt columns with diameters varying approximately between 0.48 m and 0.58 m and heights of about 2.0 m. Above these columns, a transition system formed by stone lintels transfers the gravity loads of the upper body to the columns. The main body of the minaret is approximately 13 m high and is constructed mainly from basalt stone masonry (Fig. 3). This part includes the entrance opening, internal staircase, and window openings. The wall thickness of the body is approximately 0.53 m. The upper part consists of a smaller cylindrical balcony region, followed by a conical lead-covered cap. From a structural point of view, the most critical characteristic of the minaret is the abrupt transition from the four-column base system to the relatively massive masonry body. This transition creates a significant stiffness discontinuity and causes stress concentrations under lateral seismic loading. Previous field observations reported vertical cracks in the lintel region above the columns, especially near the south-eastern and north-eastern façades, with crack widths of approximately 2–3 mm. These cracks are associated with the structural behaviour of the minaret rather than only superficial deterioration. Another important issue is the uncertainty related to the foundation system. Due to the historical and urban constraints around the monument, excavation or borehole investigations could not be performed; therefore, the exact foundation configuration remains unknown. The dimensions and structural description are consistent with the available same-monument surveys and numerical studies[34–36].

Observed damage and previous strengthening interventions

The Four-Legged Minaret is a structurally unique historical masonry monument whose seismic vulnerability is closely related to its unusual load-transfer system. Historical photographs indicate that the minaret has preserved its characteristic four-column support configuration for a long period, but the urban environment surrounding the monument has changed considerably over time (Fig. 4). The structure is not supported by a conventional continuous masonry support; instead, four independent basalt columns and a monolithic beam/lintel transition system carry the upper masonry body. This configuration gives the monument its architectural identity, while also

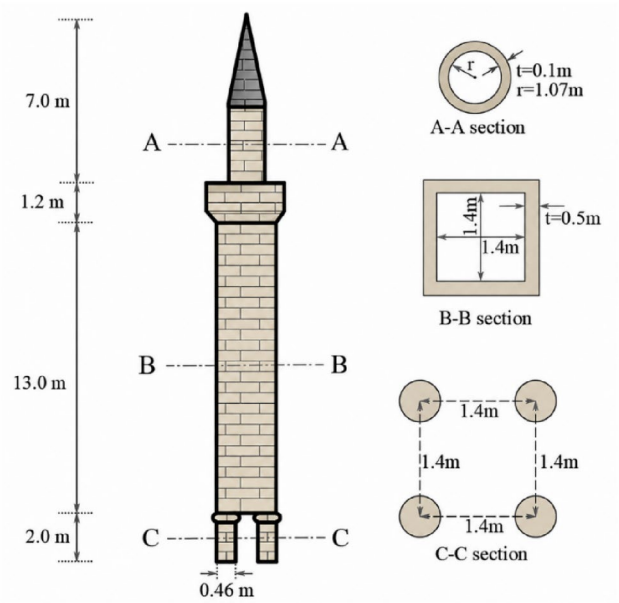


Fig. 3 Elevation, principal dimensions and cross-sections of the minaret; dimensions are in metres.

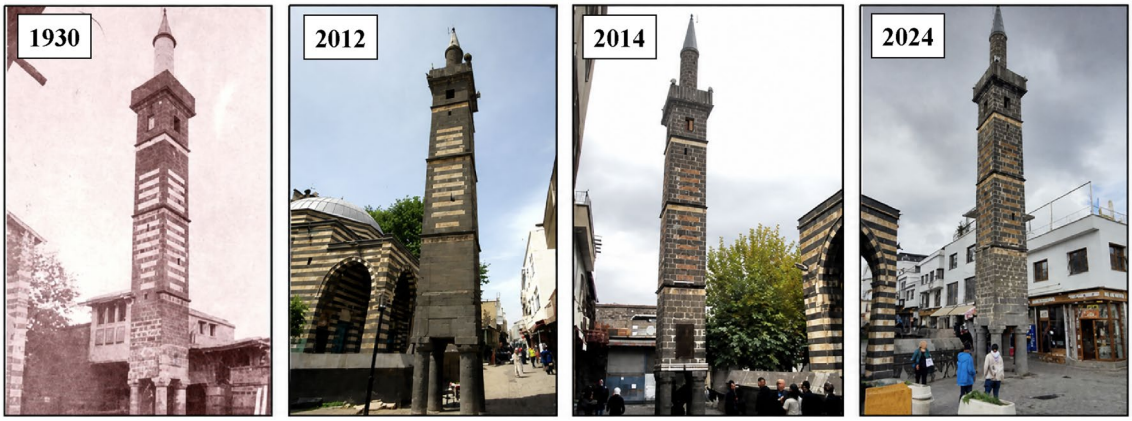


Fig. 4 Historical and recent views of the minaret (1930, 2012, 2014 and 2024). Modified after Ref.[34].

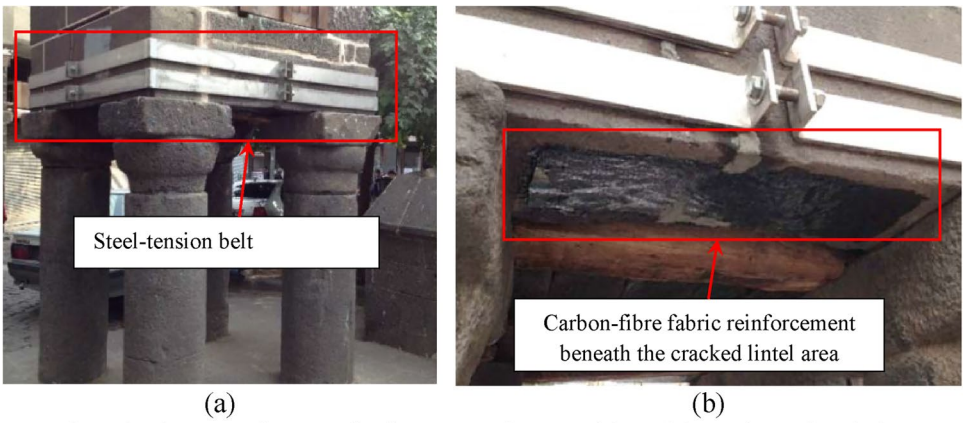


Fig. 5 Pre-earthquake interventions at the lower load-transfer transition: (**a**) steel tension-belt system and (**b**) carbon-fibre fabric beneath the cracked lintel. Modified after Ref.[34].

creating a discontinuous load path and a stiffness transition that may become critical under horizontal earthquake excitation[34].

Before the 6 February 2023 Kahramanmaraş earthquakes, the minaret had already exhibited localised damage in the lower load-transfer region. Earlier assessments reported cracks in the main lintels/beams spanning between the supporting columns, and these cracks were interpreted as structurally significant rather than purely superficial deterioration. The same studies[34,35] associated the long-term distress with a combination of possible past seismic actions, environmental degradation, uncertain foundation conditions, partial settlements, and the increasing influence of modern urban conditions such as nearby construction and traffic-induced vibrations. In particular, the proximity of the minaret to road traffic and the reduction of the original mosque courtyard area have made the lower support system more exposed to repeated dynamic actions and local serviceability-related deterioration. As part of the pre-earthquake intervention history, preventive strengthening measures were previously applied to the lower transition region. These measures included steel tension-belt applications around the base/beam region and carbon-fibre fabric reinforcement beneath the cracked lintel area (Fig. 5). These interventions were not designed to change the global structural form of the monument; rather, they aimed to improve local integrity around the cracked beam-support system and to limit further separation in the most vulnerable load-transfer zone. These prior interventions may have contributed to the relatively limited additional damage observed during the 2023 earthquake sequence[34].

During the 6 February 2023 Kahramanmaraş earthquakes, the Four-Legged Minaret sustained observable but localised damage. Field observations showed that the damage was not distributed uniformly along the height; instead, it was concentrated mainly around the lower transition, where the upper masonry body transfers its

actions to the four basalt columns through the monolithic beam and support system. The most prominent post-earthquake manifestations were vertical cracking, crack propagation through the monolithic beam above the supporting columns, and separation of masonry joints immediately above the beam. Similar mechanisms were observed on the façades (Fig. 6a), although their severity varied by direction[36]. Damage was also documented at two corners and around the supporting columns (Fig. 6b). These observations confirm a spatially non-uniform damage pattern concentrated principally at the monolithic beam, column heads and adjacent corners of the lower load-transfer transition.

The observed post-earthquake response should therefore be interpreted as the amplification of a pre-existing vulnerability mechanism rather than the formation of an entirely new damage pattern. Photographs taken before the 2023 earthquakes show vertical cracking and joint opening/deterioration in the lower beam region above the supporting columns (Fig. 7a-b). These observations are consistent with previous reports of approximately 2-3 mm wide vertical cracks near the first-row beams on the south-eastern and north-eastern façades. Accordingly, the 2023 earthquake damage can be understood as the continuation and local progression of an existing cracking and joint-separation mechanism in the lower load-transfer zone. The concentration of damage in this region is directly associated with the structural configuration of the minaret. The four independent slender columns provide vertical support, while the monolithic beam/support system transfers gravity and lateral seismic actions

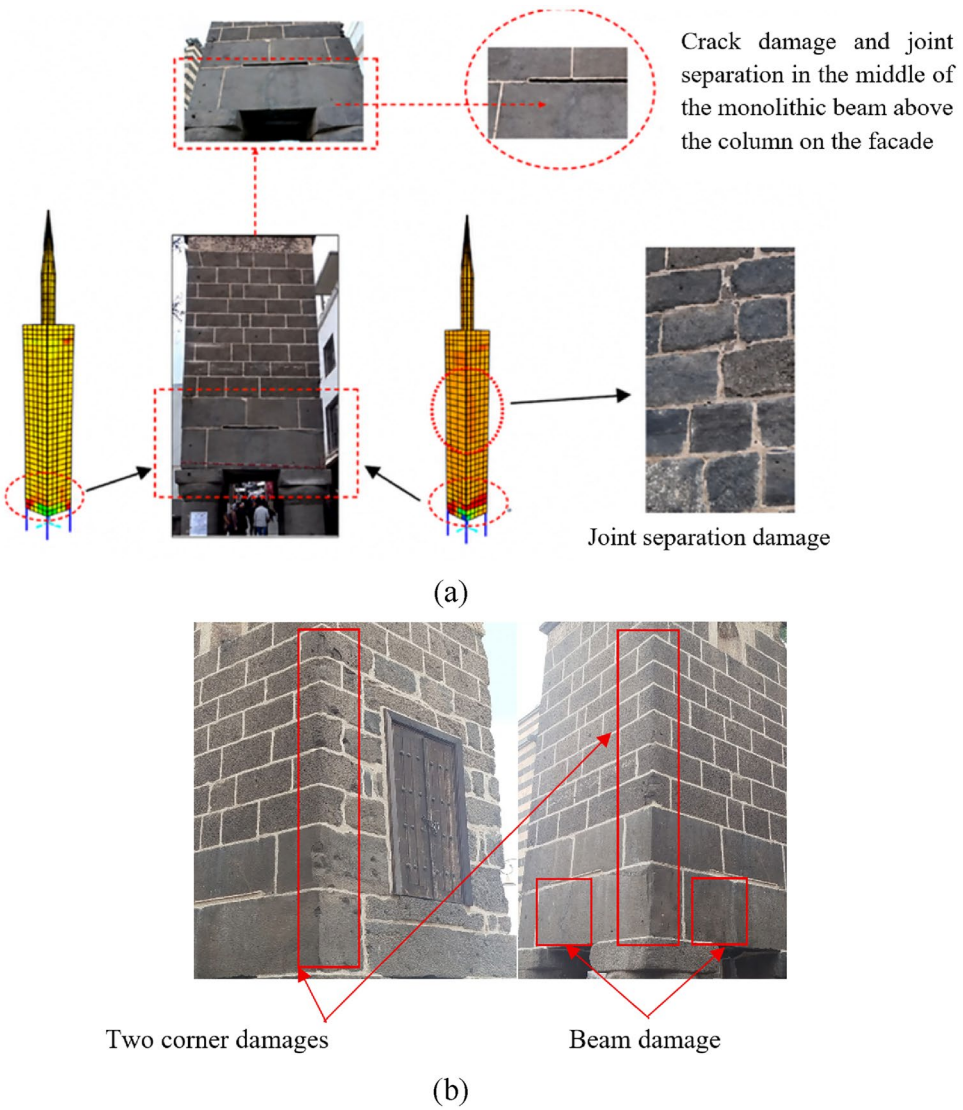


Fig. 6 Post-earthquake damage at the lower load-transfer transition: (**a**) correspondence between observed crack and joint-separation locations and the previously published nonlinear response (modified after Ref.[36]) and (**b**) local damage at the beam and column corners after the 6 February 2023 earthquakes. Photographs taken by authors.

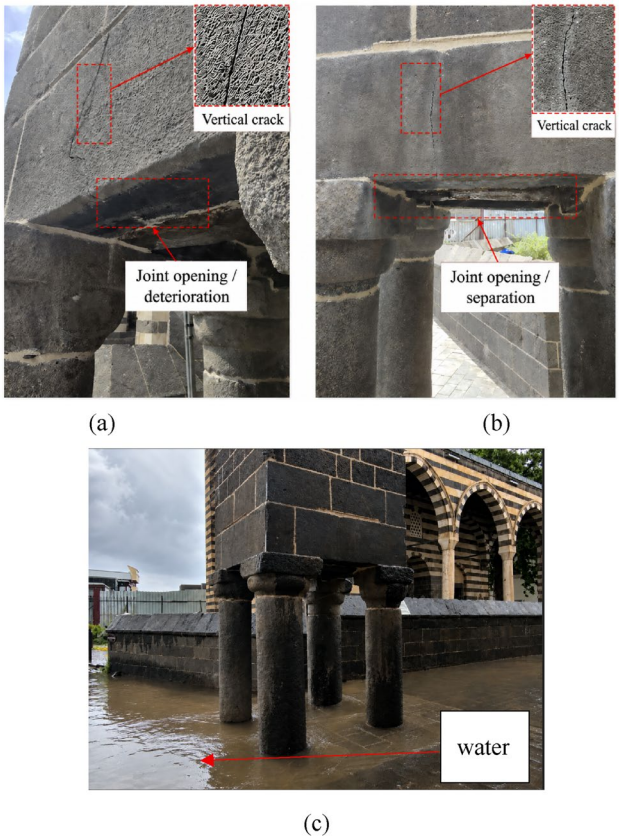


Fig. 7 Pre-earthquake condition of the lower load-transfer transition: (**a**) vertical cracking and joint opening near the beam-lintel support; (**b**) crack and joint-separation detail at a column-beam connection; and (**c**) foundation and surrounding-ground condition after heavy rainfall. Photographs supplied by the authors.

from the upper masonry body to these discrete support points. Under horizontal excitation, this abrupt change in geometry, stiffness, and load path may generate high tensile and shear stress concentrations at the column heads, monolithic beam, first-row supports, entrance/opening region, and the lower body transition zone. Numerical studies on the Four-Legged Minaret have similarly identified the base-body junction and connection regions as the most damage-prone parts of the structure[36]. Although the 2023 earthquakes caused only limited additional damage to the minaret, the existing cracked condition, the uncertain foundation configuration (e.g., Fig. 7c), the influence of surrounding urban development, and the presence of future seismic hazard in the region indicate that the structure remains vulnerable. Therefore, a comparative investigation of compatible retrofit alternatives is necessary.

In this study, global seismic-demand-reduction strategies, namely lead-rubber-bearing (LRB) and friction-pendulum-bearing (FPB) isolation, are evaluated together with local strengthening techniques comprising CFRP fabric, CFRP laminate and steel plates. This combined assessment is necessary because base isolation reduces the seismic demand transmitted to the masonry body, whereas targeted strengthening directly mitigates tensile-stress concentrations in the previously damaged lower transition. The alternatives were therefore examined to determine whether isolation alone is sufficient or whether a hybrid isolation–strengthening strategy is required to improve seismic protection and conservation planning for the Four-Legged Minaret.

Numerical modelling

Characteristics of earthquake ground motion

The minaret is located in Diyarbakır, south-eastern Türkiye, within a seismically active region influenced by the East Anatolian Fault Zone and the Bitlis–Zagros Suture Zone[38,39]. The seismic input was defined at the TBEC 2018 DD-2 ground-motion level (475-year return period)[40]. Site-specific geotechnical measurements are not available for the monument because of the historical fabric and urban constraints. Earlier studies of the same monument adopted ZC[36] and ZB[34], respectively, which demonstrates that the local site class cannot be treated as established without investigation. ZD was therefore adopted as an assumed site condition and applied identically to every configuration to provide a controlled paired comparison. It is not asserted to be the actual site class or to be uniformly more demanding than ZB or ZC over the entire period range. The reported demand levels and relative retrofit rankings are conditional on the adopted DD-2/ZD spectrum.

One real horizontal accelerogram was selected as the common seed motion: PEER NGA-West2 record RSN 1148 from the 17 August 1999 Kocaeli earthquake, recorded at the Arcelik station, ARE000 component[41]. The original PGA is 0.21008 g. The investigation was intentionally framed as a controlled deterministic paired comparison rather than a record-to-record uncertainty assessment. The same input was used for every configuration so that response changes could be attributed to the retrofit configuration. This single-record design limits statistical generalisation and does not replace a code-based multi-record assessment.

The 5%-damped TBEC 2018 DD-2/ZD target spectrum was generated from $S_s = 0.330$ and $S_1 = 0.135$[40]. For ZD, the interpolated local-soil coefficients are $F_S = 1.536$ and $F_1 = 2.330$, giving $S_{DS} = 0.5069$ g and $S_{D1} = 0.3146$ g. The resulting corner periods are $T_A = 0.1241$ s and $T_B = 0.6206$ s while the long-period transition period is $T_L = 6.0$ s. Spectral matching was performed in SeismoMatch 2024[42] using the Al Atik and Abrahamson time-domain wavelet algorithm[43]. The matching interval was 0.020–4.000 s, which covers the 0.622 s fixed-base period and the approximately 3.27–3.57 s isolated periods. The settings were mismatch tolerance = 0.300, maximum iterations = 30, initial scale factor = 1.000, minimum eigenvalue = 0.001, group size = 250, with dynamic padding enabled. The matched record was then used unchanged in every nonlinear time-history analysis.

Figure 8 compares the raw and spectrum-matched acceleration, velocity and displacement histories. The time-domain wavelet adjustment changed PGA from 0.21 to 0.23 g, PGV from 13.95 to 38.17 cm/s and PGD from 14.24 to 24.33 cm. The larger relative increases in PGV and PGD result from modification of the record's frequency content and long-period compatibility rather than from a single constant-amplitude scale factor. The Arias-intensity and velocity-pulse evaluations in Fig. 9 indicate a concentrated energy build-up at approximately 14–20 s, while Fig. 10 compares the matched response spectrum with the DD-2/ZD target. Conclusions are restricted to this selected spectrum-compatible motion; dispersion associated with duration, phase, pulse characteristics and cumulative cycling requires a future multi-record study[44].

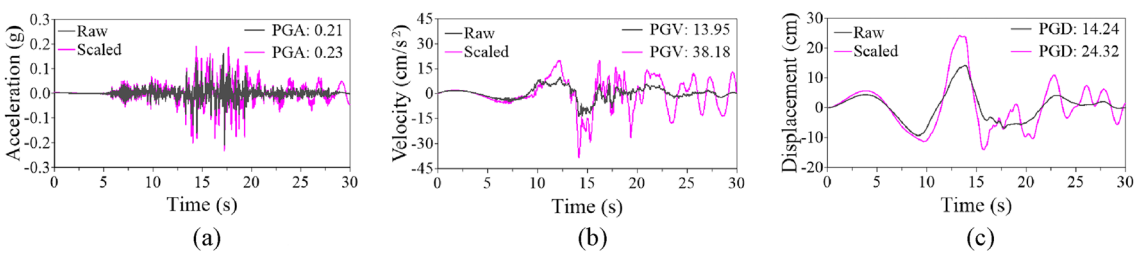


Fig. 8 Raw and spectrum-matched time histories: (**a**) acceleration (g), (**b**) velocity (cm/s) and (**c**) displacement (cm).

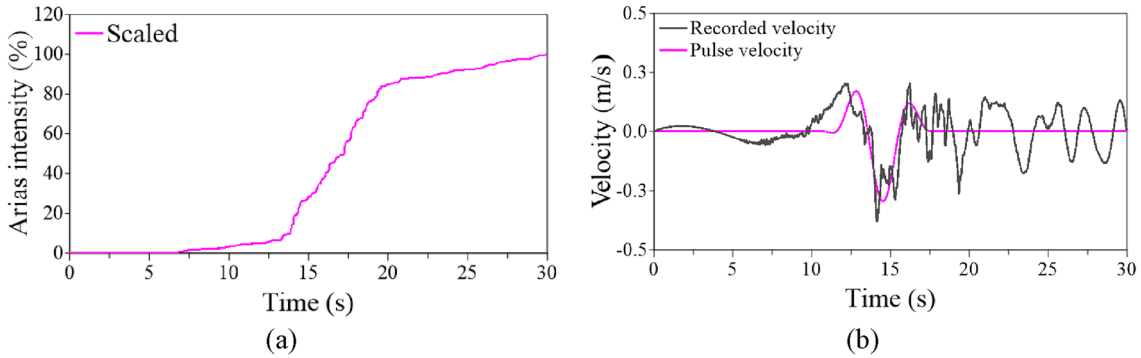


Fig. 9 Time-domain characteristics of the matched motion: (**a**) cumulative Arias intensity and (**b**) velocity history with extracted dominant pulse; time is in seconds Fig 10. Frequency-domain characteristics of the selected motion: (**a**) 5%-damped acceleration response spectrum compared with the TBEC 2018 DD-2/ZD target and (**b**) Fourier-amplitude spectrum.

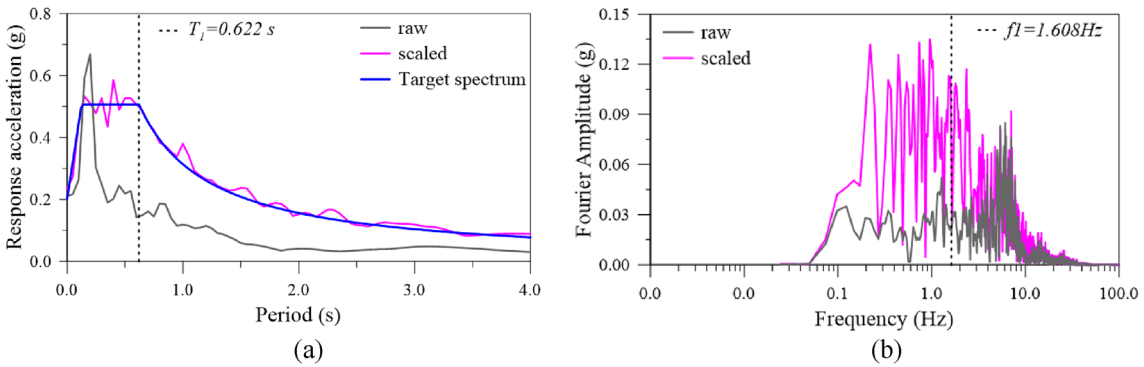


Fig. 10 Frequency-domain characteristics of the selected motion: (**a**) 5%-damped acceleration response spectrum compared with the TBEC 2018 DD-2/ZD target and (**b**) Fourier-amplitude spectrum.

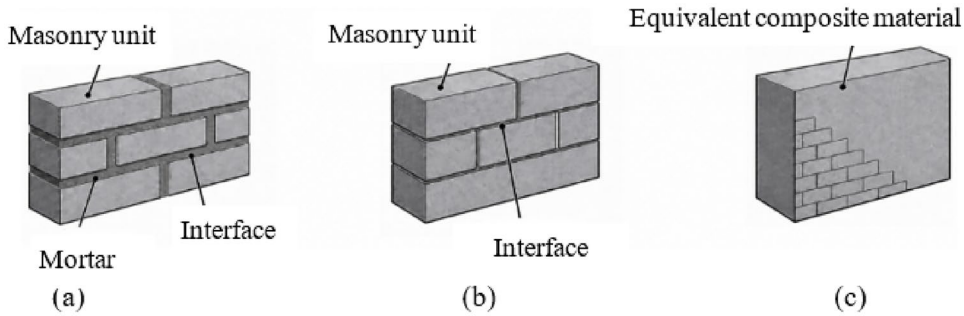


Fig. 11 Schematic representation of masonry modelling approaches: (**a**) detailed micro-modelling, (**b**) simplified micro-modelling, and (**c**) equivalent continuum macro-modelling (modified after[48]).

Material properties

Material properties in historical masonry are uncertain because of heterogeneity, ageing, weathering, previous repairs and restricted destructive testing. The equivalent-continuum model used E = 71,400 MPa and Poisson's ratio = 0.15, following the published model of the same monument[36]. The actual SAP2000 unit-weight input used here was 25 kN/m3 value reported in Ref.[36]. The present idealisation corresponds to the equivalent-continuum macro-model in Fig. 11c; basalt units, mortar joints and unit–mortar interfaces were not represented separately, and no analytical unit–mortar homogenisation was performed in this study. Values of 50 MPa in compression and 8 MPa in tension are used only as nominal monolithic/intact-basalt references, not as assigned effective capacities

of the masonry assemblage. Ref.[34] makes this distinction and reports substantially lower homogenised-body values (compressive strength 4.74 MPa, E = 3.54 GPa and a 1 MPa tensile criterion). Tests on porous Diyarbakır basalt reported approximately 51.76 MPa compression and 7.16 MPa Brazilian tension[45], whereas the lower ranges in the Italian Circular[46] concern masonry assemblages rather than intact basalt units.

The 2 MPa value used in the proposed workflow is an external, project-specific tensile-stress design-control target applied to the calculated S22 demand. It was selected as one-quarter of the nominal 8 MPa intact-basalt reference, thereby imposing a fourfold design margin for the comparative retrofit screening. The 2 MPa target is not a SAP2000 material input, measured crack-initiation threshold, code capacity or estimate of the unknown effective tensile capacity of the existing masonry assemblage. The target-to-demand performance index is $\eta_t^{(m)} = \frac{\sigma_{t,target}}{|\sigma_{t,max}^{(m)}|} \geq 1$ denotes numerical satisfaction of the adopted target. Satisfaction does not establish that cracking is impossible or that the monument is safe; lower tensile demand remains preferable, and the target must be recalibrated if site-specific testing establishes an effective assemblage capacity.

Uncertainty was not propagated probabilistically because defensible distributions are unavailable for material properties, foundation geometry, soil stiffness, existing cracks and strengthening interfaces. The fixed-foundation, equivalent-material and full-bond assumptions were therefore retained as a common baseline. Foundation flexibility or rocking could lengthen the period and alter support rotation, isolator demand and local stress transfer; the direction of the change need not be monotonic because it depends on soil stiffness and spectral content. More favourable conditions could make fewer layers sufficient, whereas lower effective tensile resistance, imperfect bond, differential settlement or stronger cyclic demand could require additional layers or a different intervention. Implementation requires geotechnical investigation, foundation identification, material characterisation and bond/anchorage verification.

3D FEM details

A three-dimensional finite element model (FEM) was developed in SAP2000[47] for comparative global and local response assessment. The adopted equivalent-continuum macro-model is the approach illustrated in Fig. 11c. Layered shell elements represent membrane and bending response, through-thickness integration and the added retrofit layers; the masonry layer components S11, S22 and S12 were assigned the user-defined nonlinear material response described below. The macro-model does not explicitly resolve individual basalt blocks, mortar joints or interfaces. Quadrilateral shells were used in regular areas and triangular shells around openings and geometric transitions. The four basalt columns, monolithic beam/lintel transition, main body, openings, balcony, upper shaft and cap were represented explicitly. The common geometry, mesh and constitutive framework were retained across the retrofit configurations. Previously installed local steel belts and deteriorated CFRP were excluded, so the reference configuration is an idealised unretrofitted benchmark rather than the as-is strengthened monument.

The model architecture has a published response-level validation history. Ref.[36] used the same monument geometry, a 922-element mesh and five through-thickness masonry integration layers, and reported convergence of the first natural frequency after approximately 900 elements. Its nonlinear analyses of the 2023 Pazarcık and Elbistan records located the highest demands at the monolithic beam, openings and lower transition, consistent with documented cracking and joint separation. The present study inherits the geometry, mesh, modal characteristics, critical-region identification and basalt stress–strain envelopes from that same-monument model. The five-layer masonry through-thickness discretisation reported for that reference model is conceptually distinct from the variable number of added CFRP retrofit plies examined here. This response-level agreement supports global behaviour and critical-region identification but is not independent validation of discrete fracture evolution. In SAP2000, material bazalt was implemented as an uncoupled user-defined uniaxial nonlinear law. The seven entered (strain, stress) pairs, with stress in MPa and compression negative, were (−0.003999, −285), (−0.002999, −210), (−0.001999, −115), (−0.0006998, −25), (−0.0004999, −10), (0, 0) and (+0.0009997, +0.25). The complete signed seven-point backbone, including the positive tensile branch, was adopted directly from the SAP2000

source model underlying the same-monument study in Ref.[36] and is reproduced here for transparency. Ref.[36] attributes its plotted basalt stress–strain curves to Xu et al.[49], whose experiments concern uniaxial compression; Ref.[49] therefore supports only the compression-side provenance and does not independently validate the tensile branch. Kinematic hysteresis was retained as the SAP2000 cyclic unloading/reloading rule, not as an independently calibrated masonry damage law. The Drucker–Prager friction and dilatation angles were both 0°, coupled nonlinear modelling was None, Von Mises plasticity was inactive and no masonry plastic hinges were assigned. The final positive coordinate is an input point of the adopted curve, not the separately imposed 2 MPa design-control target. SAP2000 extrapolates the slope of the final two points beyond the entered deformation range[50]; therefore, +0.25 MPa is an entered coordinate rather than a tensile cap. CSI describes the Kinematic rule as a model commonly used for ductile materials such as metals[51]. Its use here is consequently phenomenological and should be calibrated against masonry cyclic tests before predictive damage assessment (Fig. 12).

The homogenised continuum does not explicitly distinguish basalt blocks, mortar joints, unit–mortar interfaces or pre-existing discrete cracks. Its nonlinear material curve supplies a phenomenological direction-wise stress–strain response, and the S22 contours are interpreted as comparative demand fields and susceptibility indicators. The formulation cannot reproduce a unique mesh-independent crack path or width, joint opening, frictional sliding, separation and re-contact, block rocking, crushing-fracture evolution, post-peak localisation, fragmentation or collapse progression. It likewise does not constitute a calibrated masonry cyclic-damage law. Those mechanisms require interface/contact, micro-/meso-scale or discrete-element models and structure-specific calibration. Related nonlinear and seismic-assessment applications to other historical masonry typologies are reported in[52–57].

Full strain compatibility was assumed between the masonry and the CFRP or steel layers. Consequently, debonding, adhesive failure, anchor slip, substrate detachment, interface separation and corrosion-related deterioration were not explicitly modelled. These mechanisms may reduce the effective transfer of tensile and flexural forces and may produce higher residual masonry stresses than those predicted numerically. The reported

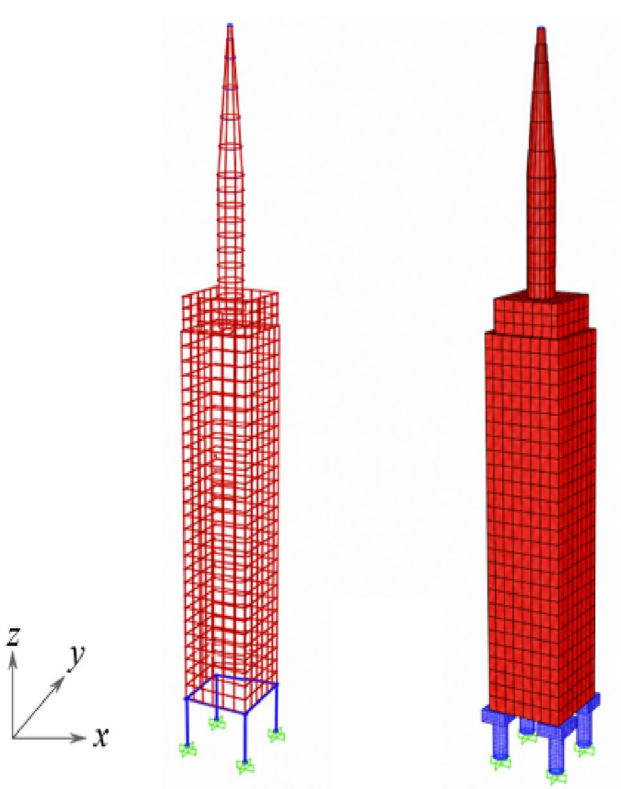


Fig. 12 Three-dimensional layered-shell finite element model of the Four-Legged Minaret.

reductions, particularly those obtained for steel plates, should therefore be interpreted as comparative upper-bound mechanical performance under idealised interface conditions rather than as directly achievable field values.

Analysis details

An NTHA requires an appropriate representation of energy dissipation. Accordingly, a 5% Rayleigh damping ratio was assigned to represent the inherent and otherwise unmodelled damping of the historical masonry superstructure. Comparable 5% damping assumptions have also been adopted in previous numerical studies of historical masonry structures[27,57–60]. The same target and the same numerical coefficients were retained in all configurations to preserve a paired comparison. Energy dissipation by the LRB and FPB devices was represented separately through their nonlinear link hysteresis or friction and was not replaced by an increased equivalent viscous ratio. This choice isolates retrofit effects but does not reproduce possible configuration-dependent changes in inherent damping. For implementation-level assessment, the damping-ratio-versus-period relationship should be checked explicitly, and superstructure damping should, where feasible, be assigned independently of the nonlinear isolator hysteresis.

$$C = \alpha M + \beta_R K \tag{1}$$

where C is the damping matrix, M is the mass matrix, K is the stiffness matrix, α is the mass-proportional damping coefficient, and β_R is the stiffness-proportional damping coefficient. The damping ratio ξ_n for a vibration mode with circular frequency ω_n can be written as

$$\xi_n = \frac{\alpha}{2\omega_n} + \frac{\beta_R \omega_n}{2} \tag{2}$$

By assigning the same target damping ratio to two selected modes and j, the Rayleigh damping coefficients are calculated as

$$\alpha = \frac{2\xi\omega_i\omega_j}{\omega_i + \omega_j}; \beta_R = \frac{2\xi}{\omega_i + \omega_j} \tag{3}$$

The first and seventh modal frequencies of the unretrofitted reference model were used to define the Rayleigh coefficients. NTHAs were performed as nonlinear direct-integration history cases in SAP2000. Each earthquake case continued from the end state of the preceding nonlinear gravity case. The same matched acceleration function was applied simultaneously in global U1 and U2 with a scale factor of 9.81 m/s^2. The integration/output time step was 0.005 s and 5999 output steps were retained. The implicit Hilber–Hughes–Taylor operator was used to control high-frequency numerical oscillation. Because direct integration solves the equations of motion in physical coordinates, the nonlinear analyses were not truncated to the seven modes displayed in the modal-results section. For f_1 = 1.608 Hz and f_7 = 7.990 Hz at 5% damping, the retained coefficients are α = 0.8411 s^{-1} and β_R = 0.001658 s. These coefficients imply approximately 24.0% Rayleigh damping at T = 3.559 s and 22.0% at T = 3.266 s; isolated-model responses may therefore include substantial long-period mass-proportional damping and require a configuration-specific damping sensitivity analysis before design use. Applying the identical ARE000 component simultaneously in global U1 and U2 represents a perfectly correlated equal-component biaxial loading scenario, not two recorded orthogonal components; directional combination, relative phase and record-to-record uncertainty were not assessed.

Geometric nonlinearity was represented through the P-Delta formulation; full large-displacement kinematics were not activated. Geometry, mass source, integration scheme, time step, boundary idealisation and seismic input were kept common to all configurations. The extracted response measures were relative and top displacement, isolator displacement, inter-storey drift ratio (IDR), stress and strain distributions, base shear, link hysteretic energy and maximum tensile stress. IDR was used only as a supplementary global-deformation indicator

because the monument does not possess a conventional multi-storey structural system. The adopted comparison framework supports relative evaluation of the retrofit alternatives but does not replace site-specific uncertainty and sensitivity studies.

Retrofitting strategies and implementation techniques

LRB as retrofitting solution

In this study, LRBs were adopted as one of the base-isolation strategies for the seismic protection of the Four-Legged Minaret. LRBs combine vertical load-carrying capacity, lateral flexibility, and hysteretic energy dissipation in a single device. They generally consist of alternating rubber and steel laminates with a central lead core, which yields under cyclic lateral deformation and provides additional damping. This mechanism allows the isolator to support the superstructure vertically while reducing the seismic demand transmitted to the masonry body by increasing the effective horizontal flexibility of the system[61,62]. The nonlinear force-displacement response of the LRB was represented by a standard bilinear hysteretic model, which is widely used for lead-rubber isolation systems[25]. In this idealization (Fig. 13), the response is described by two stiffness parameters: the elastic stiffness, K_e, and the post-yield stiffness, K_p. The elastic stiffness is defined as the ratio of the yield force, F_y, to the corresponding yield displacement, D_y, as given below:

$$K_e = \frac{F_y}{D_y} \tag{4}$$

The post-yield stiffness is related to the shear deformation of the rubber layers and is expressed as:

$$K_p = \frac{G A_r}{t_r} f_L \tag{5}$$

where G is the shear modulus of the rubber, A_r is the cross-sectional area of the rubber bearing, t_r is the total rubber thickness consisting of n individual rubber layers, and f_L is the shape or modification factor used in the LRB formulation. In the present design framework, this factor was taken as 1.5. The characteristic strength, Q, represents the horizontal-force intercept of the bilinear hysteresis loop at zero displacement. It is calculated using the lead-core area and the yield stress of the lead material as follows:

$$Q = A_{pb}\,\sigma_{ypb} \tag{6}$$

where A_{pb} is the cross-sectional area of the lead plug and σ_{ypb} denotes the yield stress of lead. The effective stiffness, K_{eff}, is defined at the selected target displacement level and is calculated as the ratio of the maximum horizontal force, F_m, to the corresponding isolator displacement, Δ:

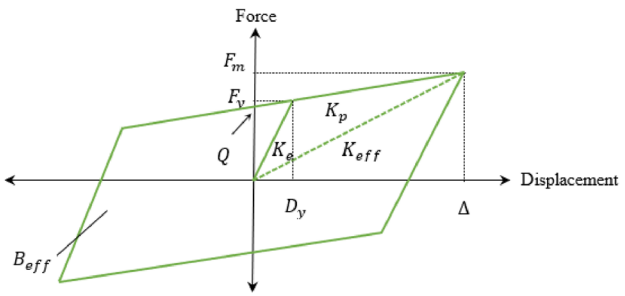


Fig. 13 The hysteresis loop of a standard bilinear LRB (modified after[25]).

$$K_{eff} = \frac{F_m}{\Delta} \tag{7}$$

The energy dissipated by the isolator during one complete loading cycle is represented by the area enclosed by the hysteresis loop, A_{loop}. For the bilinear LRB idealization, this area can be determined as:

$$A_{loop} = 4Q\left(\Delta - D_y\right) \tag{8}$$

The effective damping ratio, ξ_{eff}, is obtained by relating the hysteretic energy dissipated per cycle to the strain energy stored in the equivalent linear system. Accordingly, the equivalent viscous damping ratio is expressed as:

$$\xi_{eff} = \frac{A_{loop}}{2\pi K_{eff}\Delta^2} \tag{9}$$

The effective period of the isolated system was evaluated using the total mass of the isolated structural system and the cumulative effective lateral stiffness of the LRB devices. The period is calculated as:

$$T = 2\pi\sqrt{\frac{M}{\sum K_{eff}}} \tag{10}$$

where M is the total mass of the isolated system, including both the superstructure and the isolation mechanism, and ΣK_{eff} is the sum of the effective stiffness values K_{eff} of the LRB units. The governing equation of motion was formulated using effective and equivalent parameters, following the simplified representation commonly used for base-isolated structures[63]. Although this approach idealizes the nonlinear isolator response by equivalent quantities, it provides an efficient and sufficiently accurate representation for global response assessment of typical base-isolated systems[63]. The equation of motion is written as:

$$M\ddot{x}(t) + C_{eff}\dot{x}(t) + K_{eff}x(t) = -M\ddot{x}_g(t) \tag{11}$$

In this expression, x(t) denotes the relative displacement of the isolated structure with respect to the ground, while $\ddot{x}_g(t)$ represents the horizontal ground acceleration. The mass term M accounts for the isolated structural mass, and C_{eff} and K_{eff} represent the equivalent damping and effective stiffness of the isolation system, respectively. The effective damping coefficient is calculated from the effective damping ratio as:

$$C_{eff} = 2\xi_{eff}\sqrt{M K_{eff}} \tag{12}$$

In the numerical modelling stage, the geometric configuration and mechanical properties of the LRB units were defined according to the adopted isolation design. Following the displacement-based design philosophy (see Fig. 14) used for base-isolated systems, the design and maximum displacement demands were first established. Due to the limited clearance between the mosque's wall and the minaret, as well as the need to prevent unintended eccentric force transfer to the minaret columns, the maximum targeted isolation displacement was limited to approximately 0.08 m. Four LRB units were positioned beneath the minaret, corresponding to the four primary support locations of the lower structural system. In SAP2000, each LRB was represented using a Rubber Isolator link element as detailed in Ref.[31]. The lateral flexibility and nonlinear hysteretic behaviour of the isolation system were assigned in the two horizontal translational directions of the link, whereas the vertical load-carrying response was represented by a high-stiffness spring along the link's local vertical axis. This modelling approach enables the isolators to reduce horizontal seismic demand while maintaining adequate vertical support for the masonry superstructure.

The adopted LRB properties were selected from the manufacturer's technical catalogue[64]. The effective horizontal stiffness, elastic stiffness, yield force, post-yield stiffness, and vertical stiffness adopted in the numerical model are summarized in Table 1. These parameters were used consistently in all LRB-based models, including the standalone LRB isolation model and the hybrid LRB with CFRP and steel plate strengthening models.

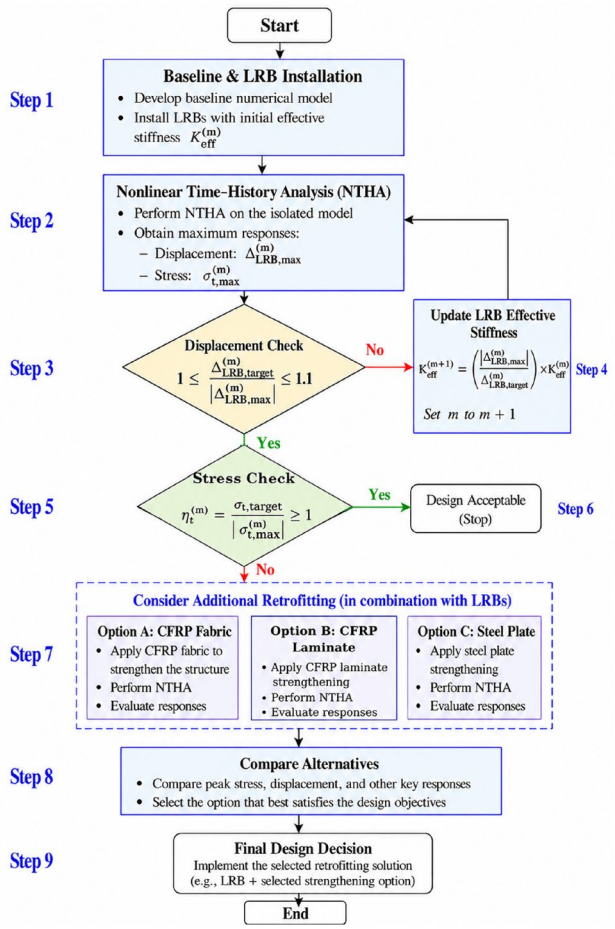


Fig. 14 LRB-based hybrid-retrofit workflow. The superscript (m) identifies the current iteration. Absolute values are used for the maximum LRB displacement and tensile-stress demand.

Table 1 Adopted LRB parameters used in the numerical model.

Parameter	Symbol	Value	Unit
Effective horizontal stiffness	K_{eff}	250	kN/m
Elastic stiffness	K_e	2300	kN/m
Yield force	F_y	20	kN
Post-yield stiffness	K_p	230	kN/m
Vertical stiffness	K_v	5800	kN/m
Adopted LRB design-control displacement	$\Delta_{LRB,target}$	0.08	m

The same LRB properties, boundary assumptions, and nonlinear link definitions were retained throughout the comparative analyses. Therefore, the response differences obtained between the unstrengthened model, LRB isolation model and the hybrid LRB with CFRP and steel plate strengthening models can be attributed directly to the adopted isolation and strengthening strategies rather than to changes in the baseline masonry properties or numerical analysis settings. The adopted value of 0.08 m is a project-specific design-control displacement and does not define the ultimate displacement capacity of the selected LRB. Device displacement capacity, stability and testing requirements must be verified in detailed design.

Proposed design methodology for LRB

Figure 14 presents the complete LRB-based hybrid-retrofit procedure. The sequence begins with the baseline model and the installation of four LRBs, continues with nonlinear time-history analysis (NTHA), and then applies

two sequential acceptance checks. The first check controls the bearing displacement and triggers an iterative stiffness update when required. The second check controls the tensile-stress demand and activates local strengthening when the adopted stress target is exceeded. The final stages compare the hybrid alternatives and select the solution that best satisfies the structural and conservation objectives. The same overall decision sequence is used for the FPB branch; Fig. 15 is retained only to distinguish the device-specific update variables and energy-dissipation mechanisms.

- Step 1 (*Baseline model and LRB installation*). The unretrofitted finite-element model is established and four LRBs are assigned with an initial effective stiffness. The symbol m denotes the current iteration, and the superscript (m + 1) denotes the subsequent iteration.
- Step 2 (*Nonlinear analysis*). An NTHA is performed using the common spectrum-matched input (or under a set of earthquake records). At each iteration, the absolute maximum LRB displacement and the absolute maximum tensile-stress demand in the critical regions are extracted. Absolute values are used because the acceptance checks depend on response magnitude rather than loading direction.
- Step 3 (*Displacement check*). The targeted displacement is compared with the absolute displacement demand obtained at the m^{th} iteration:

$$1 \leq \frac{\Delta_{\mathrm{LRB,target}}}{\left|\Delta_{\mathrm{LRB,max}}^{(\mathrm{m})}\right|} \leq 1.10 \tag{13}$$

The target-to-demand displacement ratio in equation (13) is required to remain between 1.00 and 1.10. A value below 1.00 indicates that the targeted displacement has been exceeded, whereas a value above 1.10 indicates that the selected bearing is under-utilised. If the criterion is not satisfied, the effective stiffness is updated.

Step 4 (*Stiffness update*). When the displacement check is not satisfied, the effective stiffness for the next iteration is calculated from the absolute displacement demand at iteration m:

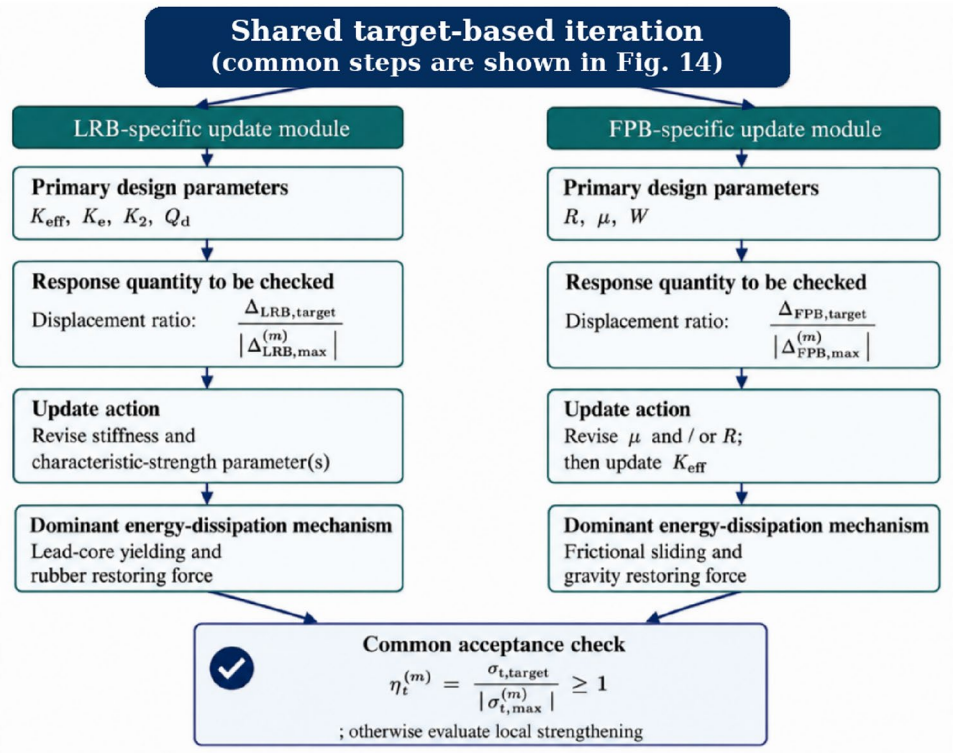


Fig. 15 Comparative schematic of the device-specific parameter-update modules embedded in the shared target-based iterative retrofit design workflow of Fig. 14. Only the differing LRB and FPB design variables, update actions and energy-dissipation mechanisms are shown.

$$K_{\text{eff}}^{(m+1)} = \left(\frac{\left| \Delta_{\text{LRB,max}}^{(m)} \right|}{\Delta_{\text{LRB,target}}} \right) \times K_{\text{eff}}^{(m)} \tag{14}$$

The effective stiffness calculated for iteration m + 1 is assigned to the LRB links, and the NTHA is repeated. This loop continues until the displacement criterion is satisfied.

Step 5 (*Tensile-stress check*). After displacement convergence, the targeted tensile-stress value is compared with the absolute maximum tensile demand at the same iteration:

$$\eta_t^{(m)} = \frac{\sigma_{\text{t,target}}}{\left| \sigma_{\text{t,max}}^{(m)} \right|} \geq 1 \tag{15}$$

The targeted tensile stress is the adopted project-specific 2 MPa design-control value. The target-to-demand performance index is satisfactory when $\eta_t^{(m)} \geq 1$ (see equation (15)). A value below unity indicates that the calculated demand exceeds the selected target and that local strengthening is required. The absolute demand makes the check independent of the shell-output sign convention. This is a comparative design-control criterion, not a material failure function; its satisfaction does not demonstrate that cracking is impossible or that the monument is unconditionally safe.

- Step 6 (*Acceptance of the isolated model*). The LRB-only configuration is accepted for the analysed scenario only when both the displacement and tensile-stress checks are satisfied.
- Step 7 (*Hybrid strengthening*). If the displacement criterion is satisfied but the tensile-stress index is below unity, CFRP fabric, CFRP laminate and steel-plate alternatives are introduced in the critical regions and re-analysed under the same seismic input.

Option A - CFRP fabric: fabric layers are applied to the critical regions, and the strengthened model is re-analysed.

Option B - CFRP laminate: laminate strips are applied to the same critical regions, and the response is evaluated under the common input.

Option C - Steel plate: steel plates are assigned to the critical regions, and their stress-reduction efficiency is evaluated.

- Step 8 (*Comparison*). The alternatives are compared using tensile stress, bearing displacement, global displacement, base shear and stress distribution, together with conservation-related criteria.
- Step 9 (*Final selection*). The retrofit alternative that best satisfies the structural and conservation objectives is selected.

Single friction pendulum bearing (FPB) as a retrofitting solution

Single friction pendulum bearings (FPBs) were evaluated as an alternative isolation system. Their lateral resistance consists of a friction component and a gravity-restoring component generated by movement along the concave surface. The governing response is therefore controlled mainly by the vertical load, friction coefficient, radius of curvature and sliding displacement.

$$F = \frac{W}{R} u + \mu W \operatorname{sgn}(\dot{u}) \tag{16}$$

Here, F is the horizontal bearing force, W is the vertical load, R is the radius of curvature, u is the sliding displacement and μ is the friction coefficient. The effective stiffness is obtained from the force-displacement relation at the selected displacement.

$$K_{eff} = \frac{W}{R} + \frac{\mu W}{D} \tag{17}$$

The total effective horizontal stiffness is the sum of the stiffness values of the four FPB units.

$$K_{eff,tot} = \sum_{k=1}^{n_b} K_{eff} \tag{18}$$

The effective period is calculated from the total isolated mass and the combined FPB stiffness.

$$T_{eff} = 2\pi\sqrt{\frac{M}{K_{eff,tot}}} \tag{19}$$

The energy dissipated by one FPB during a complete cycle is approximated from the friction force and sliding amplitude.

$$E_D = 4\,\mu\,W\,D \tag{20}$$

The corresponding equivalent damping ratio is obtained by relating the frictional energy dissipation to the strain energy of the equivalent system.

$$\xi_{eff} = \frac{E_D}{2\pi K_{eff} D^2} \tag{21}$$

These relations show that the FPB response is governed by the effective radius, friction, vertical load and sliding demand. Four Friction Isolator links were placed beneath the same support locations used for the LRB system. Along the link-local vertical U1 direction, both effective and nonlinear stiffness were 3,000,000 kN/m; the effective-damping and nonlinear damping-coefficient inputs were 0.15. Along the link-local horizontal U2 and U3 directions, effective stiffness was 293 kN/m, effective damping 0.15 and nonlinear stiffness 21,952 kN/m. The slow and fast friction coefficients were 0.05 and 0.025, the rate parameter was 1.0, the net pendulum radius was 1.15 m and the shear-deformation distance from End-J was 0 m. The P–Delta option was Shear Couple, and rotational directions R1–R3 were not assigned. Equation (21) is retained as an idealised amplitude-dependent equivalent-damping relation; the value 0.15 in Table 2 is the actual SAP2000 effective-damping input and is not presented as a back-calculated result of equation (21). These link properties represent frictional sliding and gravity restoring action; all configurations used the same input motion, model, damping definition and response measures.

The adopted value of 0.08 m is a project-specific sliding-displacement target and does not represent the ultimate displacement capacity of the FPB unit.

Proposed design methodology for FPB

The FPB branch follows the same analysis, displacement-control, stress-control and alternative-selection sequence defined in Fig. 14. The superscript (m) again identifies the current iteration. Only the device-update variable differs: the FPB response is adjusted primarily through the friction coefficient and, when required, the effective radius or bearing arrangement. Figure 15 summarises these device-specific differences.

The four FPBs were assigned beneath the principal supports. Their initial properties were defined by R, μ, W and the targeted sliding displacement (e.g., 0.08 m). All other modelling and analysis parameters were kept unchanged. The effective stiffness of one FPB at the target displacement is given by equation (22).

$$K_{eff,i}^{(m)} = \frac{w_i}{R_{effi}^{(m)}} + \frac{\mu_i^{(m)} w_i}{D} \tag{22}$$

Table 2 Adopted parameters for a single FPB unit.

μ	Target D (m)	$\mathbf{R_{eff}(m)}$	$\mathbf{K_{eff}(kN/m)}$	$\mathbf{K_{eff,tot}(kN/m)}$	β_{eff}
0.05	0.08	1.15	293	1172	0.15

The total stiffness is obtained by summing the stiffness of the four bearings.

$$K_{eff,tot}^{(m)} = \sum_{i=1}^{n_b} K_{eff,i}^{(m)} \tag{23}$$

After the initial FPB properties are assigned, an NTHA is performed. At each iteration, the absolute maximum FPB displacement and the corresponding absolute maximum tensile-stress demand are extracted.

$$1 \leq \frac{\Delta_{\mathrm{FPB,target}}}{\left|\Delta_{\mathrm{FPB,max}}^{(\mathrm{m})}\right|} \leq 1.10 \tag{24}$$

The FPB displacement check is also based on response magnitude. The absolute displacement demand is compared with the targeted sliding displacement. If the target interval is not satisfied, equation (25) first defines the effective-stiffness target for iteration m + 1. The friction coefficient is then revised—and, if necessary, the effective radius or bearing arrangement is adjusted—to realise that target in the SAP2000 link model.

$$K_{\mathrm{eff}}^{\mathrm{m+1}} = \left|\frac{\Delta_{\mathrm{FPB,max}}^{(\mathrm{m})}}{\Delta_{\mathrm{FPB,target}}}\right| K_{\mathrm{eff}}^{\mathrm{m}} \tag{25}$$

The revised friction coefficient and any associated FPB parameter changes are assigned to the subsequent iteration, and the NTHA is repeated until displacement convergence is obtained. After displacement convergence, the tensile-stress criterion is evaluated using the absolute maximum demand at the converged iteration.

$$\eta_{\mathrm{t}}^{(\mathrm{m})} = \frac{\sigma_{\mathrm{t,target}}}{\left|\sigma_{\mathrm{t,max}}^{(\mathrm{m})}\right|} \geq 1 \tag{26}$$

The targeted tensile stress is the adopted project-specific 2 MPa design-control value. The FPB-only model satisfies the numerical stress check when the target-to-demand performance index is at least unity (equation (26)); otherwise, CFRP fabric, CFRP laminate or steel plates are added at the critical regions and the hybrid model is re-analysed under the same input. Figure 15 summarises the device-specific update stages. The LRB branch is updated through bilinear stiffness and characteristic-strength parameters and dissipates energy mainly through lead-core yielding. The FPB branch is updated through friction and/or effective radius and dissipates energy through sliding, while gravity supplies restoring action. In both branches, the superscript (m) identifies the current iteration, and only the calculated demand carries this iteration index.

Figure 15 therefore complements Fig. 14 without duplicating it: Fig. 14 defines the complete procedure, whereas Fig. 15 isolates the mechanical differences between the two bearing systems. The conceptual LRB and FPB arrangements are shown in Fig. 16. Both systems are located beneath the same four supports.

CFRP fabric as retrofitting solution

CFRP fabric was assessed as a lightweight local strengthening method. In SAP2000 it was implemented as an idealised linear FIB material layer within the same layered-shell section as the nonlinear masonry layer, with material angle 0° and linear S11/S22/S12 retrofit behaviour. A one-ply definition used 0.166 mm fabric over the 500 mm lower-wall masonry section and the 100 mm upper-shaft masonry section, with no layer gap or overlap. The fibre direction was aligned with the dominant tensile-demand path[17,21,22]. Separate analysis models varied the number of added fabric plies; the equivalent fabric thickness was t_{eq} = n (0.166 mm), so the representative five-ply case used t_{eq} = 0.830 mm. The single-ply section definition is therefore one variant and does not imply that every fabric model contained one ply. The reported product properties do not constitute a complete, independently calibrated orthotropic lamina card; the numerical layer should therefore be interpreted as an idealised comparative representation.

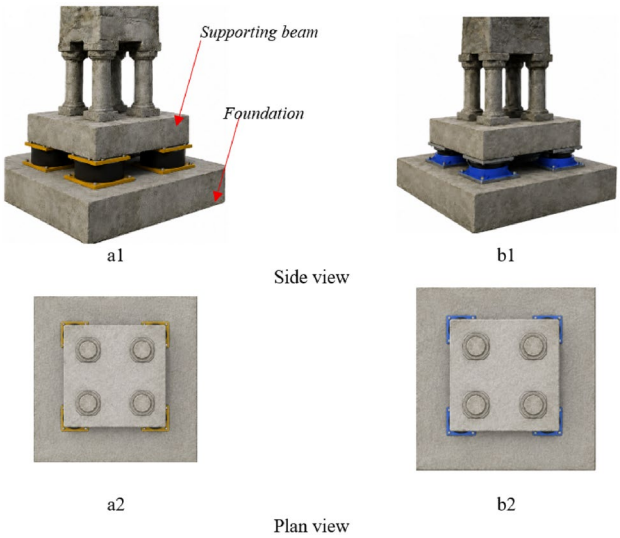


Fig. 16 Conceptual application of the base-isolation systems beneath the four support locations: (**a1**) LRB side view, (**a2**) LRB plan view, (**b1**) FPB side view and (**b2**) FPB plan view. Supporting beam and foundation are labelled; dimensions are schematic and not to scale.

$$\sigma_f = E_f \varepsilon_f; 0 \le \varepsilon_f \le \varepsilon_{fu} \tag{27}$$

Here, σ_f is the CFRP tensile stress, E_f is the elastic modulus in the fibre direction, ε_f is the tensile strain and ε_{fu} is the ultimate tensile strain.

$$f_{fu} = E_f \, \varepsilon_{fu} \tag{28}$$

For multiple layers, the equivalent CFRP thickness is obtained from the number and nominal thickness of the fabric layers.

$$t_{f,eq} = n_f \, t_f \tag{29}$$

The axial stiffness contribution is calculated from the elastic modulus and equivalent cross-sectional area.

$$(EA)_f = E_f \, \mathrm{A}_f \; \rightarrow (EA)_f = E_f \, t_{f,eq} \, b_f \tag{30}$$

The corresponding tensile-force capacity is obtained from the effective area and tensile strength.

$$(F_{fu})_f = f_{fu} \, t_{f,eq} \, b_f \tag{31}$$

CFRP fabric was assigned to the shell areas forming the lower 3.033 m column–beam–body band and the upper 2.475 m body–balcony/shaft band. Because the masonry and fabric are layers of the same shell section and share the same kinematics, full strain compatibility (perfect bond) is imposed. No separate adhesive or interface elements were used; debonding, delamination, adhesive failure, anchor slip, substrate detachment and fabric rupture were not simulated. The calculated benefit consequently represents the idealised full-bond response and requires project-specific bond and anchorage verification[23] (Table 3).

CFRP laminate as retrofitting solution

CFRP laminate was evaluated as a stiffer local strengthening alternative in the same two bands. It was represented as an idealised linear LAM material layer within the masonry layered-shell section, with material angle 0° and linear S11/S22/S12 behaviour. Each laminate ply was 1.2 mm thick; separate models used the equivalent thickness t_{eq}=n (1.2 mm), and the representative two-ply case therefore used 2.4 mm. The common layered-shell

Table 3 Material properties of CFRP fabric.

Material properties	Value	Unit
Modulus of elasticity	230000	MPa
Poisson's ratio	0.400	–
Tensile strength	4900	MPa
Design section thickness	0.166	mm
Total fibre weight	300	g/m^2
Density	1820	kg/m^3
Elongation at break	2.100	%
Width	500	mm
Fibre orientation	One-way	
Material type	Carbon	

Table 4 Material properties of CFRP laminate.

Material Properties	Value	Unit
Modulus of elasticity	165000	MPa
Poisson's ratio	0.400	–
Tensile strength	2500	MPa
Design section thickness	1.200	mm
Density	1820	kg/m^3
Elongation at break	1.500	%
Width	120	mm
Fibre orientation	One-way	
Material type	Carbon	

kinematics imposed full strain compatibility with the masonry. As for the fabric, the available product data do not provide a complete independently calibrated orthotropic material card.

$$\sigma_p = E_p \varepsilon_p; 0 \leq \varepsilon_p \leq \varepsilon_{pu} \tag{32}$$

Here, σ_p is the laminate stress, E_p is the longitudinal elastic modulus, ε_p is the laminate strain and ε_{pu} is the ultimate strain.

$$f_{pu} = E_p \, \varepsilon_{pu} \tag{33}$$

The ultimate tensile strength is obtained from the elastic modulus and ultimate strain.

$$A_p = b_p \, t_p \tag{34}$$

The axial stiffness contribution depends on the laminate modulus and cross-sectional area.

$$(EA)_p = E_p \, \mathrm{A}_p = E_p \, b_p \, t_p \tag{35}$$

The tensile-force capacity is calculated from the effective laminate area and tensile strength.

$$(F_{pu})_p = f_{pu} \, A_{pu} = f_{pu} \, b_p \, t_p \tag{36}$$

The laminate-layer count was varied in separate analysis models; the one-ply section definition and the representative two-ply result are different configurations. No adhesive/interface/slip elements were used, and debonding, delamination, adhesive failure, anchorage failure, end peeling, CFRP rupture and local substrate detachment were not represented. Because these mechanisms can govern CFRP-strengthened masonry under cyclic loading[24], the predicted reductions are interpreted as idealised full-bond effectiveness. The laminate properties used in the analysis are given in Table 4.[65]

Steel plate as retrofitting solution

Steel plates were evaluated as a high-stiffness local strengthening option and were implemented as linear S235 layers within the same layered-shell sections as the masonry. The lower 500 mm masonry wall used a 20 mm steel layer, whereas the 100 mm upper cylindrical shaft used a 10 mm steel layer; the material angle was 0° and no gap or overlap was defined. These composite sections were assigned to the selected shell areas in the lower 3.033 m and upper 2.475 m strengthening bands. Shared shell kinematics imposed perfect bond/full strain compatibility. The model captured the elastic axial and flexural contribution of the plates but did not represent mechanical-anchor response, interface slip or separation, local substrate failure, corrosion degradation or local plate buckling.

$$\sigma_s = E_s\varepsilon_s; 0 \le \varepsilon_s \le \varepsilon_y \tag{37}$$

Here, σ_s is the steel stress, E_s is the elastic modulus, ε_s is the steel strain and ε_y is the yield strain.

$$\varepsilon_y = \frac{f_y}{E_s} \tag{38}$$

A nominal bilinear post-yield relation is given for material-characterisation context; the steel retrofit layers used in the reported layered-shell analyses were assigned linear component behaviour.

$$\sigma_s = f_y + E_t\left(\varepsilon_s - \varepsilon_y\right); \varepsilon_y \le \varepsilon_s \le \varepsilon_{su} \tag{39}$$

For a plate of width b_s and thickness t_s, the effective area is A_s

$$A_s = b_s t_s \tag{40}$$

The axial stiffness contribution is $E_s A_s$

$$(EA)_s = E_s\,\mathrm{A}_s \tag{41}$$

The corresponding tensile yield capacity $(F_y)_s$ is as follows

$$(F_y)_s = f_y\,\mathrm{A}_s \tag{42}$$

For repeated plates or layers, the equivalent thickness is obtained from the number of plate components.

$$t_{s,eq} = n_s t_s \tag{43}$$

These relations define the tensile contribution of the steel plates in the strengthened regions. The results represent idealised full-bond performance and should not be interpreted as a detailed anchorage design. Steel plates provide the highest local stiffness among the investigated strengthening alternatives, but they also introduce greater mass, anchorage demand, corrosion risk and visual intervention. Their performance was therefore assessed together with the conservation criteria summarised in Table 9. The assigned S235 steel properties are listed in Table 5. S235 is defined in EN 10025-2[66]; the adopted elastic modulus, yield strength, Poisson's ratio and density were used in the numerical model.

Results and discussion

Modal characteristics of the numerical models

Twelve eigenmodes were extracted. The first two modes are the dominant horizontal bending modes: $T_1 = 0.622\text{s}$, $f_1 = 1.608\text{Hz}$, and $T_2 = 0.620\text{s}$, $f_2 = 1.613\text{Hz}$. Their close frequencies indicate similar lateral flexibility in the two

Table 5 Material properties of S235 steel.

Material properties	Value	Unit
Modulus of elasticity	210000	MPa
Poisson's ratio	0.300	–
Density	7850	kg/m^3
Shear modulus	80769.23	MPa
Coefficient of thermal expansion	0.0000117	$°C^{-1}$
Minimum yield stress	235	MPa
Minimum tensile strength	360	MPa
Expected yield stress	258.5	MPa
Expected tensile strength	396	MPa

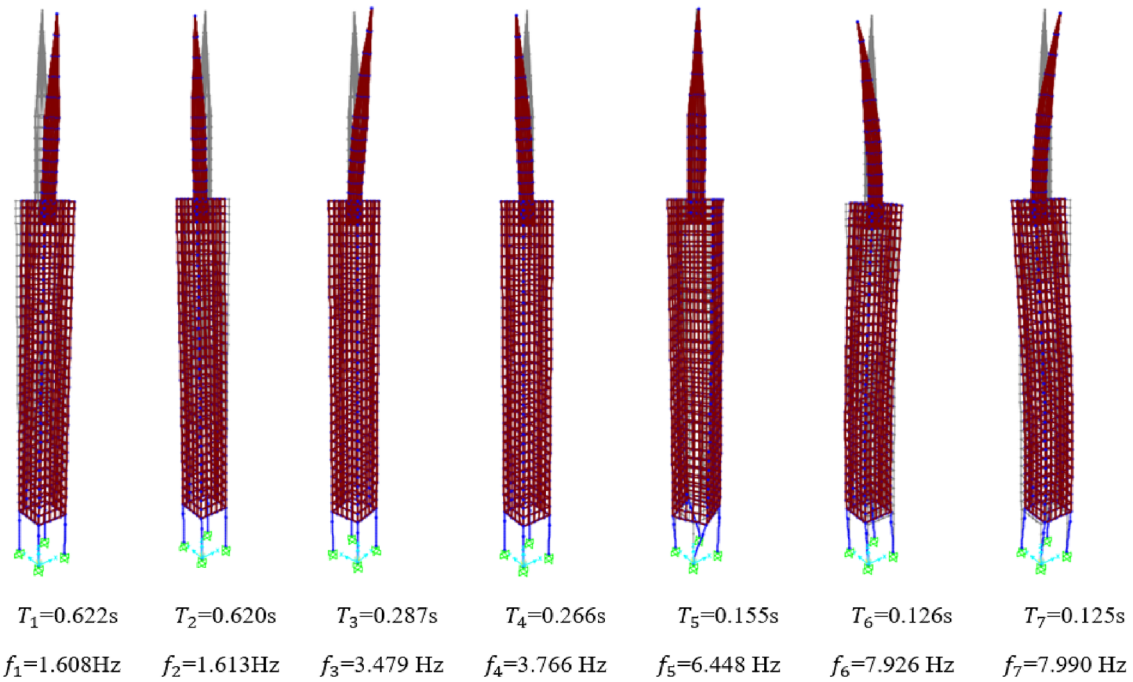


Fig. 17 Selected modal deformation patterns and frequencies of the unretrofitted reference model; displacement amplitudes are normalised mode-shape ordinates. The reference model represents an idealised unretrofitted configuration and excludes the previously installed local steel-belt and CFRP interventions.

principal directions. Modes 6 and 7 provide important additional horizontal participation and exhibit higher-order deformation patterns. However, no mode-by-mode stress decomposition was performed; therefore, the transition-zone stress concentration is established from the nonlinear time-history stress fields and field-damage correlation rather than from modal participation alone (Fig. 17).

The cumulative modal mass ratios are reported for all 12 extracted modes in Table 6. Mode 1 contributes 72.6% in U1 and mode 2 contributes 73.3% in U2. Mode 6 adds approximately 20.1% in U2, raising the cumulative U2 ratio to 98.2%; mode 7 adds approximately 20.7% in U1, raising the cumulative U1 ratio to 98.3%. Thus, the first seven modes capture more than 95% of the horizontal modal mass. Vertical participation becomes significant at mode 10 and reaches 95.5% by mode 12. These ratios justify presentation of the first seven modes for horizontal modal interpretation; they do not truncate the direct-integration NTHAs.

Table 6 Frequencies and cumulative modal mass participation ratios of the first 12 modes.

Mode	Frequency (Hz)	Cumulative U1	Cumulative U2	Cumulative U3
1	1.608	0.726	0.000	0.000
2	1.613	0.726	0.733	0.000
3	3.479	0.775	0.733	0.000
4	3.766	0.775	0.781	0.000
5	6.448	0.775	0.781	0.000
6	7.926	0.775	0.982	0.000
7	7.990	0.983	0.982	0.000
8	15.873	0.983	0.985	0.000
9	16.393	0.985	0.985	0.000
10	20.000	0.985	0.985	0.950
11	20.833	0.997	0.985	0.955
12	20.833	0.997	0.997	0.955

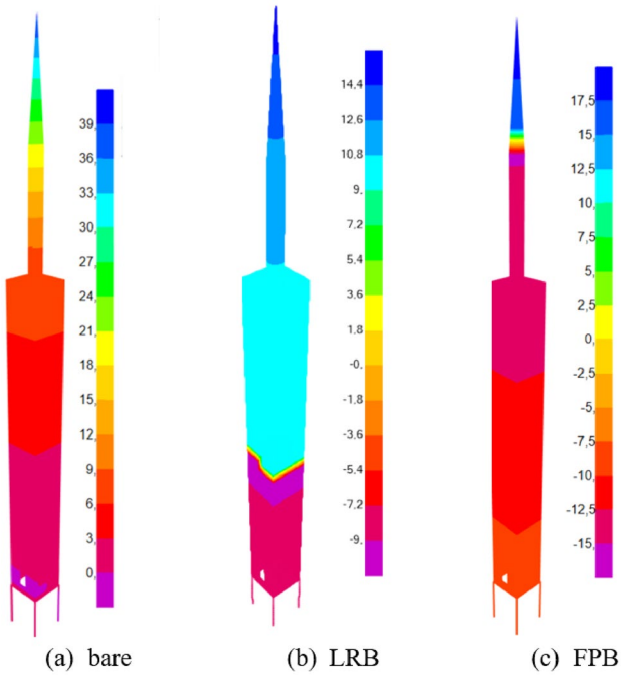


Fig. 18 Relative displacement along the minaret height in the X (U1) direction for the unretrofitted reference, LRB and FPB models; displacement is in cm.

Comparative seismic response of the unretrofitted reference, LRB-isolated and FPB-isolated models

Displacement response

As specified in the LRB and FPB design-methodology subsections, the maximum targeted bearing displacement was restricted to approximately 0.08 m for both the LRB and FPB systems due to the limited clearance around the mosque–minaret interaction zone and to avoid undesirable eccentric force transfer to the minaret columns. Therefore, the displacement response of the isolated models should be evaluated not only in terms of the reduction in superstructure displacement but also with respect to the bearing displacement limit adopted in the isolation design. The relative displacement distributions in the X and Y directions are presented in Figs. 18 and 19, respectively, for the unretrofitted reference, LRB-isolated, and FPB-isolated minaret models. In the unretrofitted reference model, the displacement demand increases progressively along the height of the minaret, indicating a typical cantilever-type response of the slender masonry body. The maximum relative displacement reaches approximately 39 cm in the X direction and 31.2 cm in the Y direction. These large displacement demands indicate that the unretrofitted minaret is highly vulnerable to horizontal seismic excitation, particularly in the upper

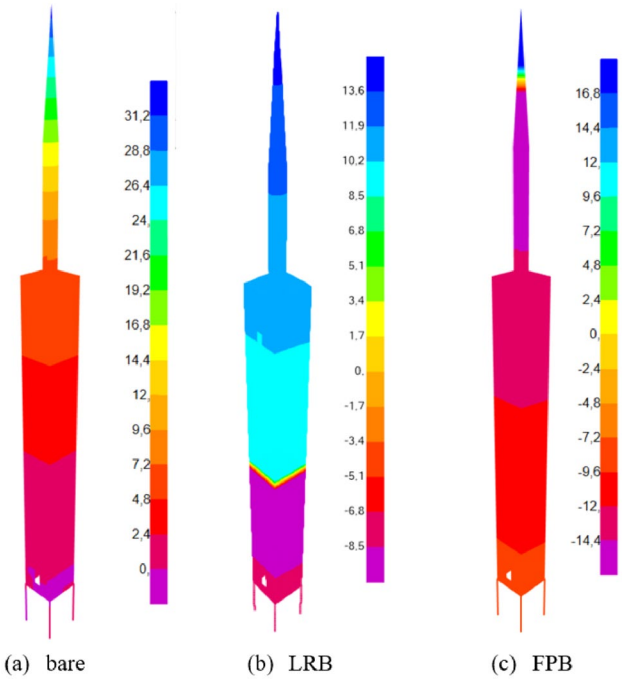


Fig. 19 Relative displacement along the minaret height in the Y (U2) direction for the unretrofitted reference, LRB and FPB models; displacement is in cm.

shaft and cap regions. In addition, the abrupt change in the displacement distribution near the lower transition region reflects the stiffness discontinuity between the four-column support system and the main masonry body.

The introduction of base-isolation systems significantly modifies the displacement response of the minaret. In the X direction, the LRB model reduces the maximum relative displacement from approximately 39 cm to 14.4 cm, corresponding to a reduction of about 63%. In the same direction, the FPB model decreases the peak displacement to approximately 17.5 cm, corresponding to a reduction of about 55%. Similarly, in the Y direction, the maximum displacement decreases from 31.2 cm in the unretrofitted reference model to approximately 13.6 cm and 16.8 cm in the LRB and FPB models, respectively. These values correspond to reductions of about 56% for the LRB model and 46% for the FPB model. These results indicate that both isolation systems are effective in reducing the displacement transmitted to the masonry superstructure while satisfying the displacement-based constraints defined by equations (13) and (24). However, the LRB system provides a slightly greater reduction than the FPB system in both principal directions. This behaviour can be attributed to the combined lateral flexibility and hysteretic energy dissipation capacity of the LRB units. The FPB system also provides a considerable improvement compared with the unretrofitted reference model, but its displacement-reduction efficiency remains relatively lower than that of the LRB model under the considered input motion.

Overall, Figs. 18 and 19 show that both isolation strategies provide substantial global-response reduction for the Four-Legged Minaret. Because the targeted bearing displacement was limited to approximately 0.08 m in the design methodology for both isolation systems, the selected LRB and FPB properties should be interpreted as displacement-constrained retrofit solutions rather than unconstrained isolation designs. This distinction is important for heritage monuments, where clearance, architectural compatibility and local force-transfer conditions at the support level may govern practical feasibility, particularly for geometrically atypical structures such as the Four-Legged Minaret.

Inter-storey drift ratio as a supplementary global-response indicator

The inter-storey drift ratio (IDR) results in Fig. 20 are presented with the global displacement response because IDR is a deformation measure rather than a local tensile-stress criterion. Levels a-d denote the support region,

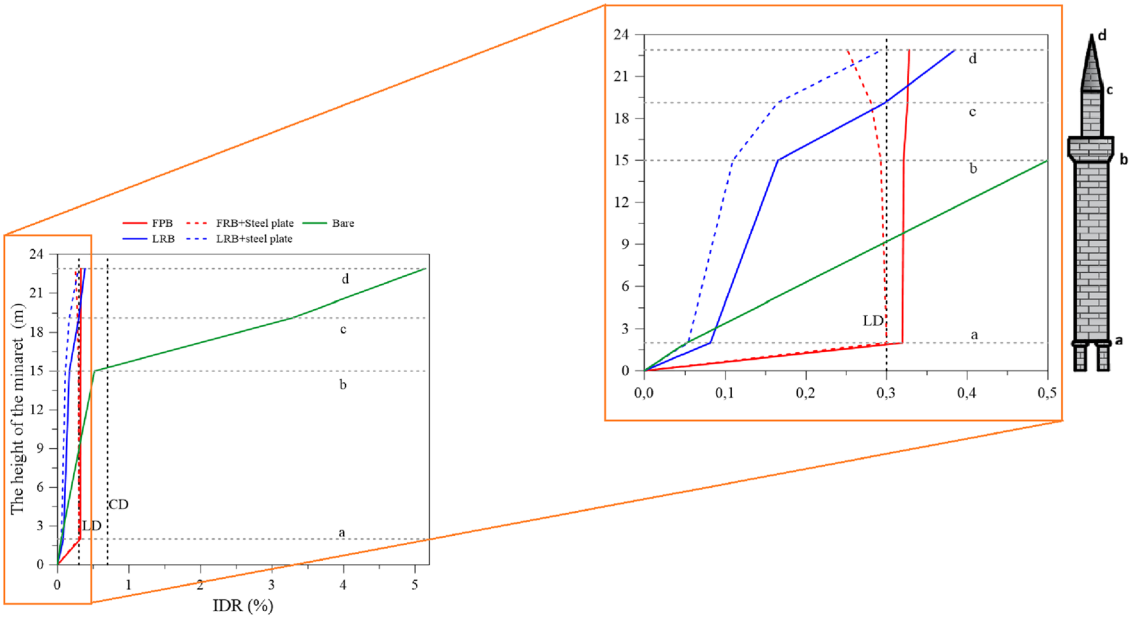


Fig. 20 Inter-storey drift-ratio distributions along the height for the unretrofitted reference, LRB, FPB, LRB + steel plate and FPB + steel plate models. The horizontal reference lines indicate the ERMGHB[67] limited-damage, controlled-damage and collapse-prevention levels; IDR is dimensionless and plotted as a percentage.

main body, balcony transition and upper shaft. The enlarged panel permits comparison of the low-drift retrofit responses.

The Earthquake Risk Management Guide for Historic Buildings[67] gives reference drift levels of 0.3% for limited damage, 0.7% for controlled damage and 1.0% for collapse prevention; similar thresholds were used in the minaret fragility study of Ref.[68]. These values are used only for comparative interpretation because the Four-Legged Minaret is not a conventional storey-based system. Tensile stress remains the primary local indicator.

As shown in Fig. 20, the unretrofitted reference model exhibits the largest IDR demand among all numerical configurations. The drift demand increases significantly along the height of the minaret and reaches values far beyond the LD and CD reference limits. This indicates that the unretrofitted structure is highly vulnerable to lateral deformation demand under the considered earthquake excitation. The excessive drift response of the unretrofitted reference model can be attributed to the slender geometry of the minaret and the abrupt stiffness and load-path discontinuity between the four-column support system and the upper masonry body. The LRB and FPB isolation systems considerably reduce the IDR demand compared with the unretrofitted reference model. Nevertheless, the drift response of the isolated models shows different damage tendencies. In the LRB-isolated model, the IDR demand is generally reduced, but the upper part of the minaret still approaches or locally exceeds the LD reference limit. This indicates that local deformation demand remains critical near the upper transition and shaft regions. In the FPB-isolated model, the drift demand appears to be more distributed along the height, suggesting a more global deformation tendency when FPB isolation is used without additional local strengthening. Therefore, although both isolation systems improve the response compared with the unretrofitted reference model, isolation alone does not completely eliminate the drift-based vulnerability of the minaret. For this reason, the steel-plate hybrid cases—which produced the lowest tensile demands inside the strengthened zones—were also compared in terms of IDR response. The results show that steel plate strengthening further controls the drift demand and shifts the response toward the LD reference range. In particular, the LRB + steel plate model exhibits the most favourable IDR distribution, with drift values remaining generally within or close to the limited-damage region along the height of the minaret. The FPB + steel plate model also provides a clear improvement compared with

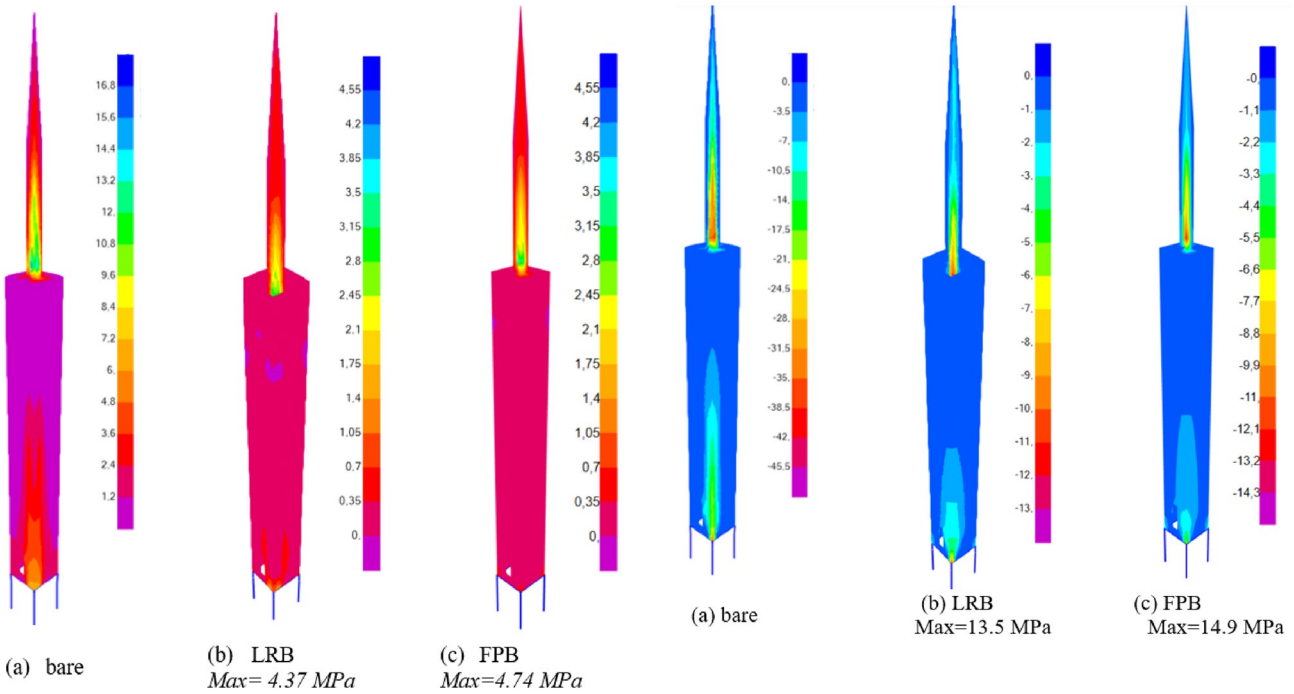


Fig. 21 Maximum tensile S22 shell stress (MPa) in the (**a**) unretrofitted reference, (**b**) LRB and (**c**) FPB models.

Fig. 22 Minimum (compressive) S22 shell stress (MPa) in the (**a**) unretrofitted reference, (**b**) LRB and (**c**) FPB models.

the FPB-only model, indicating that the addition of local strengthening effectively controls the drift concentration observed in the isolated configuration.

The unretrofitted reference model has the largest IDR, while both isolation systems reduce the global deformation. The LRB + steel plate and FPB + steel plate configurations provide further control in the selected cases. These results support the global-response benefit of the hybrid systems, but the drift thresholds should not be interpreted as structure-specific calibrated damage limits.

Compressive and tensile stress response

The maximum tensile and compressive S22 shell stress distributions obtained from the nonlinear time-history analyses are presented in Figs. 21 and 22, respectively. These results provide important insight into the local stress concentration mechanisms of the four-legged masonry minaret and the effectiveness of the isolation systems in reducing stress demands in the critical regions. The lower tensile-stress concentration is caused by the discontinuous load path: overturning moment and horizontal shear from the massive upper body are transferred through the monolithic beam/lintel to four discrete columns. The abrupt changes in support continuity, section, stiffness and effective load-transfer area produce local compatibility demands at column heads, lintels, corners and openings. This mechanism agrees with the documented cracks and joint separations and with the published field-correlated model[36].

The upper concentration has a different mechanical origin. At the balcony–shaft transition, the wall thickness and section modulus decrease; for a given bending moment, the nominal bending stress ($\sigma = M/W$) therefore increases, and the local curvature becomes larger. The inertia of the balcony and upper shaft, together with

higher-order deformation, may further amplify this transition response. Isolation reduces global force transfer but cannot fully eliminate geometry-controlled local demand.

The compressive S22 fields in Fig. 22 are concentrated in the lower body and transition, where gravity and lateral actions are transferred to the four columns. The peak compressive demands are approximately 13.5 MPa for LRB and 14.9 MPa for FPB. Although these values are below the nominal 50 MPa intact-basalt reference, that comparison cannot establish the crushing safety of the heterogeneous masonry assemblage; Ref.[34], for example, reports a much lower homogenised-body compressive strength. Because the adopted macro-model does not explicitly simulate crushing-fracture evolution or post-peak localisation, the compressive contours are used only for comparative demand assessment. Tensile-demand control remains the focus of the present retrofit screening, not a claim that compression-related damage is impossible.

Overall, Figs. 21 and 22 show that the largest local design-control exceedances in the isolated models occur in tension. The FPB model produced the lower tensile demand in the lower transition, whereas the LRB model produced a slightly lower demand in the upper transition and dissipated more link hysteretic energy under the selected motion. The governing tensile demands of both isolation-only models exceed the adopted 2 MPa project-specific design-control target. Targeted strengthening is therefore required at the critical regions within this analysed scenario. This target-based comparison does not establish an absolute failure boundary for the masonry.

Compressive and tensile strain response

The maximum tensile and minimum compressive S22 shell strain distributions are presented in Figs. 23 and 24, respectively. These strain results are consistent with the stress distributions discussed previously and provide further evidence regarding the deformation-sensitive regions of the four-legged masonry minaret under seismic excitation. As shown in Fig. 23, the unretrofitted reference model exhibits relatively high tensile strain concentrations in the lower transition region, particularly around the column heads, beam–body connection, and lower masonry body. This response confirms that the discontinuous load-transfer mechanism between the four independent supporting columns and the upper masonry body leads to local tensile deformation demands.

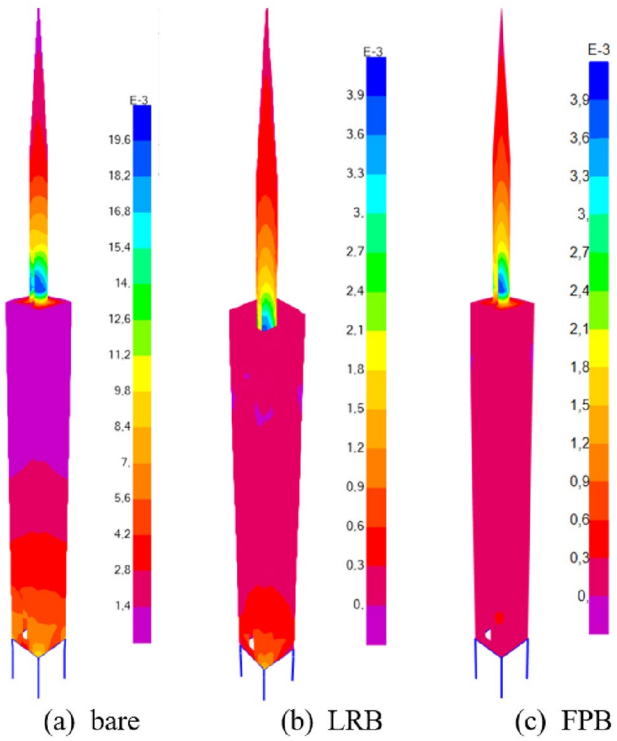


Fig. 23 Maximum tensile S22 shell strain (dimensionless) in the (**a**) unretrofitted reference, (**b**) LRB and (**c**) FPB models.

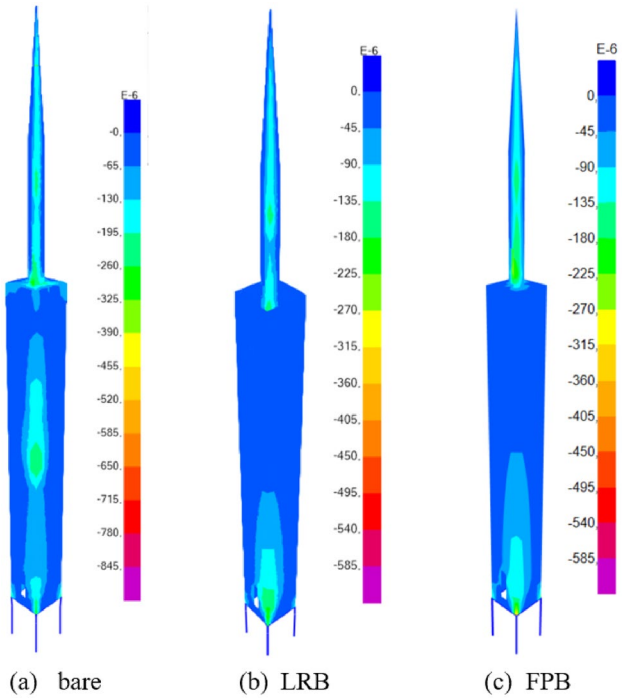


Fig. 24 Minimum compressive S22 shell strain (dimensionless) in the (**a**) unretrofitted reference, (**b**) LRB and (**c**) FPB models.

Tensile strain concentrations are also observed along the upper shaft and conical cap, indicating the contribution of global bending deformation to the overall response. However, the most critical strain accumulation remains concentrated near the base and transition zone, which is consistent with the observed cracking and joint-opening patterns reported in the field (see[36]).

The LRB and FPB isolation systems significantly reduce the tensile strain demand compared with the unretrofitted reference model. In both isolated models, the tensile strain distribution becomes more localised and less severe along the main masonry body. This indicates that the isolation systems are effective in filtering the seismic input transmitted to the upper structure and reducing deformation demand in the masonry body. Among the two isolation alternatives, the LRB model exhibits a slightly more favourable tensile strain response, with a lower and more confined strain concentration around the lower transition region. The FPB model also improves the response compared with the unretrofitted reference configuration, although relatively higher tensile strain concentrations remain visible around the transition zone and upper shaft.

The minimum compressive S22 shell strain distributions shown in Fig. 24 indicate that compressive strain demand is mainly concentrated in the lower body and transition region of the minaret. In the unretrofitted reference model, compressive strains extend over a larger portion of the masonry body, reflecting the direct transfer of seismic demand from the base to the upper structure. In contrast, both the LRB and FPB systems reduce the extent and intensity of compressive strain propagation along the height of the minaret. The isolated models show a more limited compressive strain concentration near the support and lower body regions, confirming that base isolation reduces not only stress demand but also deformation demand in the masonry components.

Overall, Figs. 23 and 24 demonstrate that the strain response of the four-legged minaret is governed primarily by the lower transition region, where stiffness discontinuity and concentrated load transfer occur. The observed strain patterns support the stress-based findings presented in Figs. 21 and 22. Although both isolation systems reduce tensile and compressive strain demands compared with the unretrofitted reference model, the LRB configuration provides a slightly more effective reduction and a more controlled strain distribution. Nevertheless, the persistence of local tensile strain concentrations around the lower transition zone indicates residual deformation susceptibility in the already damaged regions; because discrete fracture is outside the model scope, this response is not interpreted as a prediction of crack initiation or propagation. Therefore, the use of additional local

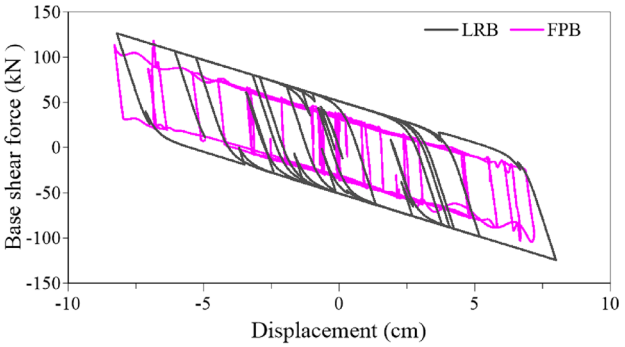


Fig. 25 Base-shear force versus bearing displacement for the LRB and FPB systems.

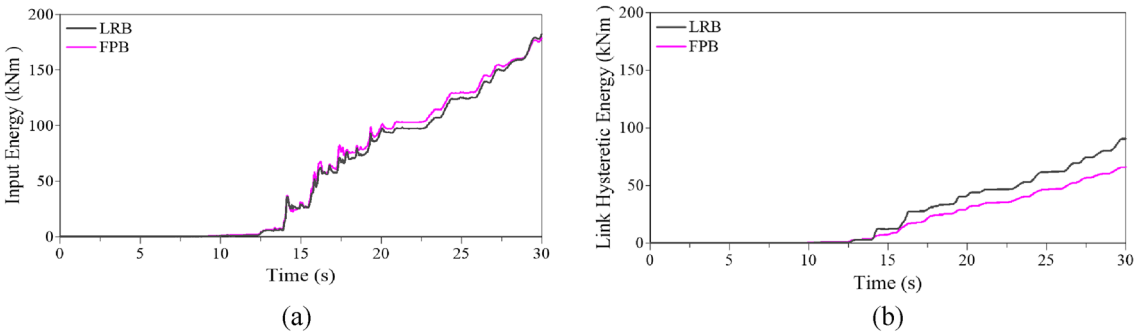


Fig. 26 Energy histories of the LRB- and FPB-retrofitted models: (**a**) input energy and (**b**) link hysteretic energy.

strengthening measures, such as CFRP fabric, CFRP laminate, or steel plate applications, should be considered to further control tensile deformation demands in the critical transition region.

Hysteretic response and energy dissipation of the isolation systems

The hysteretic force–displacement response and energy response histories of the LRB- and FPB-retrofitted minaret models are presented in Figs. 25 and 26, respectively. These results provide a direct comparison of the nonlinear behaviour of the two isolation systems under the same ground-motion excitation and within the displacement-constrained design framework adopted in this study. As specified in the LRB and FPB design-methodology subsections, the maximum targeted bearing displacement was limited to approximately 0.08 m due to the restricted clearance around the mosque–minaret interaction zone and the need to prevent unintended eccentric force transfer to the supporting minaret columns. Therefore, the comparison of the two isolation systems should be interpreted by considering that both systems reached a similar bearing displacement demand of approximately 8 cm.

Figure 25 shows the base shear force–displacement hysteresis curves of the LRB- and FPB-retrofitted models. Both systems exhibit stable nonlinear cyclic behaviour within the displacement range of approximately ±8 cm. The LRB model develops wider and more stable hysteretic loops, indicating a more pronounced energy dissipation mechanism. This behaviour is mainly associated with the yielding of the lead core and the cyclic deformation capacity of the rubber layers. The relatively larger enclosed loop area of the LRB response indicates that a greater portion of seismic energy is dissipated at the isolation level. In contrast, the FPB model exhibits a narrower and more friction-dominated hysteretic response. Although the FPB system effectively limits the base shear demand through sliding action and period elongation, its loop area is smaller than that of the LRB system, indicating a relatively lower hysteretic energy dissipation capacity under the considered displacement demand.

Hysteretic energy is the area enclosed by the force-displacement loop. In the adopted LRB model, repeated yielding of the lead core sustains a broad bilinear resisting force while the rubber supplies restoring stiffness. In

the FPB, irreversible energy is governed mainly by the frictional resistance μW; the curvature-dependent gravity term supplies restoring force but does not produce net energy over a complete cycle. Under the selected device parameters and similar approximately 0.08 m displacement demands, the LRB loop encloses a larger area. This is a parameter- and excitation-dependent result, not a universal superiority of LRB devices.

Overall, Figs. 25 and 26 demonstrate that both LRB and FPB systems can control the displacement demand within the targeted range while reducing the seismic demand transmitted to the masonry superstructure. However, the LRB system shows a more favourable response in terms of hysteretic loop stability and cumulative energy dissipation. The FPB system also contributes to seismic demand reduction through frictional sliding, period elongation, and restoring action, but its dissipated hysteretic energy remains lower than that of the LRB system. These findings are consistent with the displacement, stress, and strain results discussed previously, where the LRB-retrofitted model generally exhibited slightly better seismic response reduction than the FPB-retrofitted model.

Comparative evaluation of local strengthening strategies for tensile-stress reduction

The local strengthening models used the same masonry, ground-motion and analysis assumptions. CFRP fabric, CFRP laminate and steel were added as retrofit layers within the corresponding composite layered-shell sections. The masonry layer components S11/S22/S12 were nonlinear, while the retrofit-layer components were linear. Shared shell nodes imposed full strain compatibility; no separate epoxy or mechanical interface was modelled. Delamination, CFRP rupture, adhesive damage, anchor slip, substrate detachment and steel-interface failure were outside the model scope.

Based on the stress contour diagrams obtained from all numerical models, tensile stress concentrations were found to occur mainly in two distinct regions; therefore, local strengthening applications were implemented in these areas. The first region corresponds to the lowest part of the minaret body resting on the four supporting piers, with a height of 3.033 m. The second strengthened region extends over a height of 2.475 m around the upper body–balcony transition, as illustrated in Fig. 27. It should be noted that the dark-blue regions shown in Fig. 27, and similarly in Fig. 28, represent the locations where the strengthening materials were applied; therefore, these regions should be interpreted as strengthened zones rather than as stress contour values.

The selected area assignments cover two strengthening bands: the lower 3.033 m region and the upper 2.475 m body–balcony/shaft region. The five-ply fabric (0.830 mm) and two-ply laminate (2.4 mm) models were used. This retrofit-ply count is separate from the five-layer masonry through-thickness discretisation reported for the reference model in Ref.[36]. The steel layered sections used 20 mm in the lower wall and 10 mm in the upper shaft. All added layers were connected to the masonry through the full-bond/shared-kinematics idealisation.

The maximum tensile stress values obtained for the LRB-isolated model are summarised in Table 7. In the unstrengthened LRB-isolated configuration, the maximum tensile stresses are 2.741 MPa in the lower critical region and 4.375 MPa in the upper critical region. Both values exceed the adopted 2 MPa tensile-stress design-control target, indicating that LRB isolation alone is insufficient to satisfy the selected local comparison criterion. The greater demand in the upper region is associated with its 10 cm wall thickness, greater slenderness and lower sectional rigidity relative to the lower region, where the wall thickness is approximately 50 cm. CFRP-fabric, CFRP-laminate and steel-plate strengthening produced substantial reductions in both regions.

According to Table 7, the CFRP fabric strengthening system reduces the maximum tensile stress in the bottom region from 2.741 MPa in the unstrengthened LRB-isolated model to 2.656 MPa with one CFRP fabric layer and further to 1.685 MPa with five CFRP fabric layers. This corresponds to an overall stress reduction of approximately 38.5% relative to the unstrengthened LRB-isolated model. In the top region, the maximum tensile stress decreases from 4.375 MPa to 1.529 MPa with a single CFRP fabric layer and to 1.122 MPa with five CFRP fabric layers, corresponding to reductions of approximately 65.0% and 74.35%, respectively. These high reduction ratios demonstrate the effectiveness of CFRP fabric strengthening, particularly in the thin-section upper region where tensile stress concentration is more pronounced.

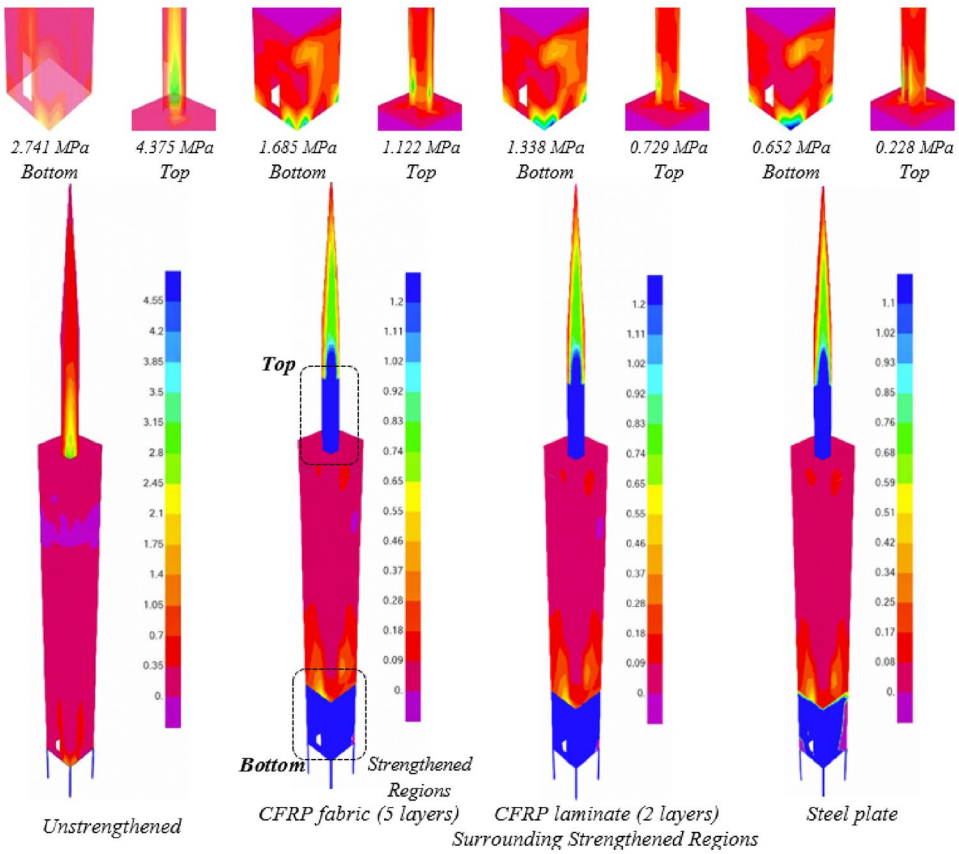


Fig. 27 Maximum tensile S22 stress contours (MPa) for the unstrengthened and locally strengthened LRB-based models.

The tensile stress falls below the adopted 2 MPa design-control target when three or more CFRP-fabric layers are used in the lower region, whereas one layer is sufficient in the upper region under the analysed motion and model assumptions. The incremental benefit decreases as the number of layers increases, indicating stiffness saturation and stress redistribution. Additional layers may also increase susceptibility to delamination, fibre rupture, adhesive damage and bond deterioration, although these mechanisms were not represented explicitly in the full-bond model.

Table 7 also shows that the CFRP laminate system provides a more efficient tensile stress reduction with fewer layers compared with the CFRP fabric system. A single layer of CFRP laminate reduces the maximum tensile stresses to 1.674 MPa in the bottom region and 1.062 MPa in the top region. These values are very close to those obtained using five layers of CFRP fabric, indicating that CFRP laminate can achieve a comparable strengthening effect with fewer layers. When two CFRP laminate layers are used, the tensile stress further decreases to 1.338 MPa in the bottom region and 0.729 MPa in the top region. These values correspond to stress reduction ratios of 51.19% and 83.34%, respectively, relative to the unstrengthened LRB-isolated model. This response can be attributed to the higher axial stiffness and tensile capacity of CFRP laminate systems, which are associated with their greater thickness and more concentrated tensile load-carrying capacity. In addition, reducing the required number of layers may help limit the risk of layer-dependent local failure mechanisms such as delamination, fibre rupture, and adhesive damage, which may become more critical in multi-layer CFRP fabric applications.

Among the alternatives in Table 7, steel-plate strengthening provides the largest numerical reduction in maximum tensile stress inside the strengthened regions. The lower- and upper-region values decrease to 0.652 MPa and 0.228 MPa, respectively, corresponding to reductions of approximately 76% and 95% relative to the unstrengthened LRB-isolated configuration. Both values are well below the adopted 2 MPa tensile-stress design-control target. The reduction arises primarily from the high effective axial and flexural stiffness of the plate, which attracts a larger share of the tensile demand. Its application to a heritage monument must nevertheless be assessed

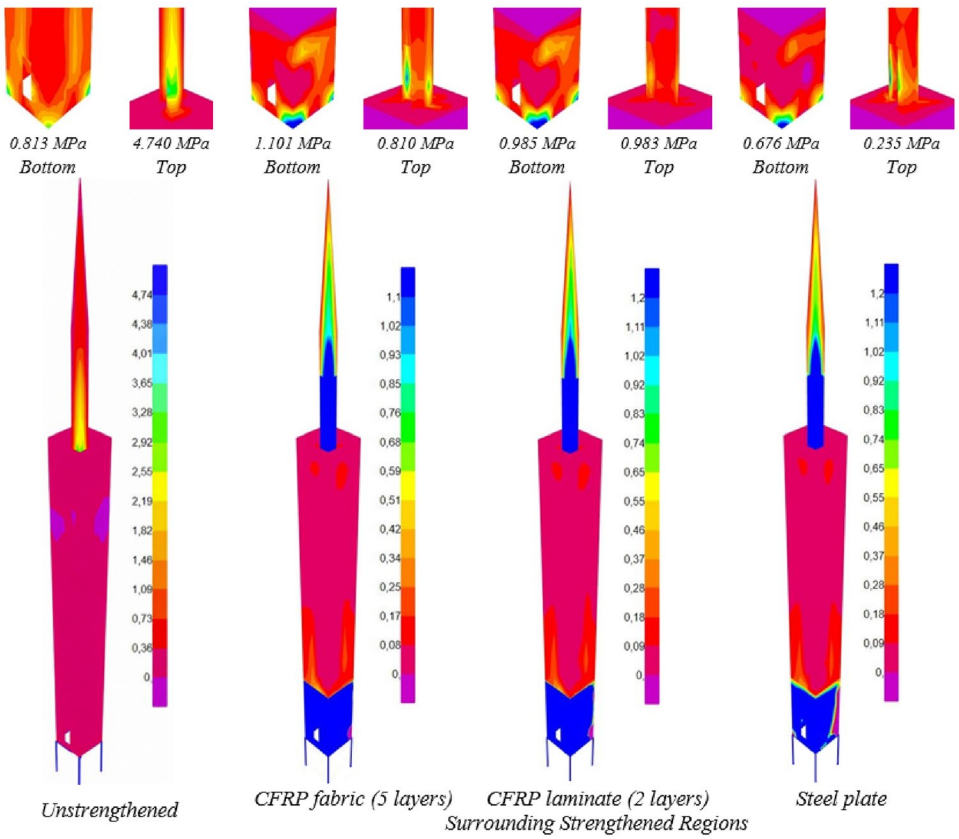


Fig. 28 Maximum tensile S22 stress contours (MPa) for the unstrengthened and locally strengthened FPB-based models. Dark-blue overlays identify the applied strengthening zones and are not stress values.

Table 7 Maximum S22 tensile stresses (MPa) in the LRB-based configurations under the selected spectrum-compatible motion.

Strengthening techniques	Maximum tensile stresses (S22) [MPa]				*Period[s]*
	Strengthened regions		Surrounding strengthened regions		
	Bottom	Top	Bottom	Top	
LRB only (no local strengthening)	**2.741**	**4.375**	–	–	**3.55934**
CFRP fabric (1 layer)	2.656	1.529	0.432	1.059	3.56378
CFRP fabric (2 layers)	2.346	1.294	0.439	1.107	3.56368
CFRP fabric (3 layers)	1.828	1.148	0.440	1.171	3.56358
CFRP fabric (4 layers)	1.747	1.120	0.427	1.188	3.56348
CFRP fabric (5 layers)	1.685	1.122	0.442	1.200	3.56339
CFRP laminate (1 layer)	1.674	1.062	0.435	1.203	3.56344
CFRP laminate (2 layers)	1.338	0.729	0.498	1.278	3.56307
Steel plate	0.652	0.228	0.444	1.194	3.57194

Significant values are in bold.

in terms of added mass, anchorage intervention, corrosion protection, visual impact, removability and compatibility with the original masonry.

Table 7 also shows slight tensile-stress increases in the masonry immediately adjacent to the strengthened zones. The local stiffness increase redistributes part of the seismic demand toward the surrounding, relatively more flexible material. All surrounding-region values remain below the adopted 2 MPa tensile-stress design-control target, but this finding confirms that local retrofit design should evaluate both the strengthened area and the neighbouring masonry. The associated period variation remains below 1%, indicating that the local interventions reduce critical stresses without materially changing the global dynamic characteristics of the LRB-isolated model.

The maximum tensile stress contour diagrams obtained for the unstrengthened LRB-isolated model and the LRB-isolated models strengthened with five layers of CFRP fabric, two layers of CFRP laminate, and steel plate are presented in Fig. 27. The contour distributions are consistent with the numerical results summarized in Table 7. In Fig. 27, the dark-blue regions shown in the strengthened models indicate the locations where the local strengthening materials were applied. Therefore, these regions should be interpreted as strengthened zones rather than as direct stress contour magnitudes. The figure confirms that local strengthening effectively reduces tensile stress concentrations in both the bottom and top critical regions, with the most pronounced reduction inside the applied zones obtained in the steel plate model.

The corresponding FPB-based results are summarised in Table 8. In the unstrengthened FPB-isolated configuration, the maximum tensile stress is 0.813 MPa in the lower region and 4.740 MPa in the upper region. Thus, the lower region already satisfies the adopted 2 MPa tensile-stress design-control target, whereas the upper region does not. The FPB system therefore controls demand effectively at the lower transition under the selected motion, but additional local strengthening remains necessary in the slender upper region.

The principal trends observed for the LRB-based alternatives are also evident in the FPB-based models. Steel plate again provides the largest numerical stress reduction inside the strengthened zones. Although tensile stresses in the surrounding regions increase slightly with strengthening level, all remain below the adopted 2 MPa tensile-stress design-control target. The structural period varies by less than 0.4%, from 3.269 s to 3.277 s, showing that local strengthening reduces critical tensile demand without materially changing the dominant isolated period of the FPB-isolated model.

The main difference between the LRB- and FPB-based responses occurs in the lower strengthened region. The unstrengthened FPB-isolated model already has a lower-region tensile stress of 0.813 MPa. CFRP application increases this value to 1.101–1.242 MPa for fabric and 0.985–1.095 MPa for laminate because the locally stiffened zone attracts a somewhat larger share of tensile demand. These values nevertheless remain below the adopted 2 MPa comparison target; the increase is therefore acceptable within the specific performance framework and modelling assumptions used in this study.

The maximum tensile stress contour diagrams obtained for the unstrengthened FPB-isolated model and the FPB-isolated models strengthened with five layers of CFRP fabric, two layers of CFRP laminate, and steel plate are presented in Fig. 28. The contour diagrams are consistent with the numerical results reported in Table 8. Similar to Fig. 27, the dark-blue regions in Fig. 28 indicate the locations where local strengthening was applied, rather than the magnitude of tensile stress. The contour results show that the stress concentration in the upper slender region is significantly reduced after the application of CFRP fabric, CFRP laminate, and steel plate strengthening. Among these alternatives, the steel plate provides the largest numerical reduction inside the applied zones, while CFRP laminate achieves an efficient stress reduction with a limited number of layers. CFRP fabric also provides satisfactory stress reduction, particularly when multiple layers are used.

Table 8 Maximum S22 tensile stresses (MPa) in the FPB-based configurations under the selected spectrum-compatible motion.

Strengthening Techniques	Maximum tensile stresses (S22) [MPa]				Period [s]
	Strengthened regions		Surrounding strengthened regions		
	Bottom	Top	Bottom	Top	
FPB only (no local strengthening)	**0.813**	**4.740**	-	-	**3.26560**
CFRP fabric (1 layer)	1.242	1.108	0.410	0.933	3.27042
CFRP fabric (2 layers)	1.205	0.944	0.453	1.030	3.27030
CFRP fabric (3 layers)	1.162	0.732	0.490	1.066	3.27019
CFRP fabric (4 layers)	1.131	0.681	0.502	1.086	3.27008
CFRP fabric (5 layers)	1.101	0.810	0.497	1.142	3.26997
CFRP laminate (1 layer)	1.095	0.825	0.492	1.141	3.27002
CFRP laminate (2 layers)	0.985	0.983	0.515	1.231	3.26957
Steel plate	0.676	0.235	0.461	1.199	3.27674

Significant values are in bold.

Table 9 Results-informed multi-criteria comparison of the representative local strengthening alternatives.

Criterion	CFRP fabric	CFRP laminate	Steel plate
Representative analysed configuration	Five layers	Two layers	Adopted plate layout
All-region governing maximum S22 in LRB hybrid	1.685 MPa; 61.5% reduction	1.338 MPa; 69.4% reduction	1.194 MPa; 72.7% reduction
All-region governing maximum S22 in FPB hybrid	1.142 MPa; 75.9% reduction	1.231 MPa; 74.0% reduction	1.199 MPa; 74.7% reduction
Adopted 2 MPa design-control target	Numerically satisfied in both isolation branches under the analysed scenario	Numerically satisfied in both isolation branches under the analysed scenario	Numerically satisfied in both isolation branches under the analysed scenario
Target-to-demand performance index, ηt, at 2 MPa	LRB: 1.19; FPB: 1.75	LRB: 1.49; FPB: 1.62	LRB: 1.68; FPB: 1.67
Effect on isolated period (LRB / FPB)	3.563 / 3.270 s; changes +0.11% / +0.13%	3.563 / 3.270 s; changes +0.10% / +0.12%	3.572 / 3.277 s; changes +0.35% / +0.34%
Added structural mass	Very low	Low	Highest of the three
Durability, corrosion and maintenance	No electrochemical corrosion; resin and concealed bond require environmental protection and monitoring	No electrochemical corrosion; resin and laminate ends require protection and monitoring	Corrosion protection and periodic inspection are required; deterioration is generally more visible
Constructability and geometric adaptability	Conforms well to irregular surfaces, but five-layer application increases curing and workmanship demand	Two layers reduce installation stages, but precise strip alignment and surface preparation are required	Lifting, fitting and anchorage are more intrusive and require greater access
Reversibility, interface risk and visual impact	Low reversibility with conventional epoxy; debonding or substrate detachment may be hidden; low visual impact when concealed	Low reversibility with conventional epoxy; end debonding and stiffness concentration require detailing; low-to-moderate visual impact	Potentially removable with mechanical connections, but anchors disturb masonry; anchor slip, local crushing and moderate-to-high visual impact
Masonry and heritage compatibility	High geometric compatibility and minimum thickness; multiple layers reduce practical efficiency	Favourable balance of low mass, limited layers and mechanical efficiency if bond and end detailing are verified	Lowest strengthened-zone demands, but least compatible where minimal intervention, corrosion avoidance and visual integrity govern
Results-informed selection implication	Lowest all-region maximum in the FPB branch; favoured where irregular geometry and conformability govern	Most balanced preliminary conservation-oriented option for the present case	Lowest all-region maximum in the LRB branch and lowest strengthened-zone demand in both branches; preferred where local stress reduction outweighs intervention impacts

Table 9 combines the all-region governing S22 maxima—defined as the largest value across the strengthened regions and surrounding masonry—with isolated-period changes and conservation criteria for the representative hybrids. Under LRB, the governing maxima are 1.685 MPa for five-ply CFRP fabric, 1.338 MPa for two-ply CFRP laminate and 1.194 MPa for steel; under FPB, the corresponding values are 1.142, 1.231 and 1.199 MPa. These values produce 2 MPa target-to-demand indices of 1.19/1.75 for LRB/FPB plus fabric, 1.49/1.62 for LRB/FPB plus laminate and 1.68/1.67 for LRB/FPB plus steel; the isolation-only indices remain 0.46 and 0.42. Accordingly, all six representative hybrids satisfy the adopted target in both strengthened and surrounding

regions under the analysed scenario, whereas the two isolation-only configurations do not. The isolated periods change by less than 0.4%.

A threshold-sensitivity check was performed using these all-region governing S22 maxima without re-running the analyses. At a 1 MPa target, none of the representative hybrids satisfies the criterion simultaneously in the strengthened and surrounding regions. At 2 and 4 MPa, all six hybrids satisfy it, whereas LRB only (4.375 MPa) and FPB only (4.740 MPa) do not. At 8 MPa, the two isolation-only cases also satisfy the criterion. Because the calculated demands do not change, the numerical ordering within each isolation branch is independent of the selected target; only the binary compliance classification changes. This confirms that compliance is threshold-dependent.

When these numerical outcomes are considered together with added mass, durability, constructability, reversibility, interface risk, visual impact, maintenance and masonry compatibility, three distinctions emerge: local efficiency inside the applied bands, all-region governing performance and conservation-oriented selection. Steel plates produce the lowest stresses inside the strengthened zones in both isolation branches. After adjacent-region redistribution is included, however, no single alternative has the lowest all-region maximum in both branches: steel is lowest for LRB (1.194 MPa), while fabric is lowest for FPB (1.142 MPa). CFRP laminate remains the most balanced preliminary conservation-oriented alternative because the representative two-layer configuration combines compliance with the 2 MPa target, low added mass and limited visual intervention. CFRP fabric remains advantageous where conformity to irregular masonry surfaces is decisive, although five layers were used in the representative comparison. Steel plate is most appropriate where maximum reduction inside the strengthened bands governs and where anchorage disturbance, corrosion protection, added mass and visual impact can be accepted. The final selection remains subject to site-specific bond or anchorage verification and multidisciplinary heritage review. No numerical weighting or aggregate score was assigned because stakeholder priorities and implementation details are project-specific; Table 9 is therefore a results-informed screening matrix rather than a formal optimisation.

Conclusions

A comparative assessment of global isolation, local strengthening and hybrid retrofit strategies was conducted for the historical Four-Legged Minaret using a common three-dimensional layered-shell model and a DD-2/ZD spectrum-compatible ground motion. Within the adopted numerical framework, the principal conclusions are as follows:

- The largest local tensile demands occur at two geometric discontinuities. At the lower transition, overturning moment and horizontal shear pass from the masonry body to four discrete basalt columns through the beam–lintel system. At the upper balcony–shaft transition, the reduced wall thickness and section modulus increase local curvature and bending-induced tensile demand. The compressive contours were lower than the nominal intact-basalt reference but were not used to claim crushing safety, because the effective masonry assemblage capacity is uncertain and crushing-fracture evolution is outside the macro-model.
- Both lead-rubber-bearing (LRB) and friction-pendulum-bearing (FPB) isolation reduced the displacement, drift and distributed stress demands of the masonry superstructure. However, isolation alone did not control all local tensile stresses. Maximum S_{22} demands of 2.741 and 4.375 MPa were obtained in the lower and upper critical regions of the LRB model, respectively, whereas the corresponding FPB values were 0.813 and 4.740 MPa. For the selected device parameters and motion, the LRB system dissipated more link hysteretic energy than the FPB system, yet this result should not be interpreted as a general superiority of LRB devices.
- Targeted strengthening reduced the all-region governing tensile demand below the adopted 2 MPa project-specific design-control target in all representative hybrid configurations under the selected motion. For CFRP fabric, CFRP laminate and steel, respectively, the governing maxima were 1.685, 1.338 and 1.194 MPa in the

LRB branch and 1.142, 1.231 and 1.199 MPa in the FPB branch. Steel produced the lowest stresses inside the applied bands (0.652 and 0.676 MPa), but adjacent masonry governed the all-region response in several configurations. Satisfaction means only that the calculated demand is below the selected target for this scenario; it is not proof of crack prevention or unconditional safety. Changes in isolated period remained below 0.4%, indicating primarily local stress redistribution.

- Numerical effectiveness alone is insufficient for selecting an intervention for a historical monument, and no single alternative minimised the all-region maximum in both isolation branches. Steel plates produced the lowest demands inside the strengthened zones but introduced greater mass, anchorage demand, corrosion-protection requirements and potential visual and physical impact. CFRP laminate provided the most balanced preliminary combination of target compliance, low added mass and limited installation stages, whereas CFRP fabric retained an advantage for irregular masonry surfaces and yielded the lowest all-region maximum in the FPB branch. Final selection must therefore integrate structural performance with compatibility, durability, constructability, inspectability, maintenance and heritage significance.
- The results support a hybrid retrofit framework in which isolation is used to reduce the seismic demand transmitted to the monument and local strengthening is applied only where geometry-controlled tensile concentrations remain. This separation of global and local response mechanisms provides a rational basis for comparing retrofit alternatives for structurally irregular masonry monuments.

The reported stress levels, layer requirements and rankings are conditional on one spectrum-matched motion, the assumed DD-2/ZD spectrum, the equivalent-continuum properties, fixed-foundation conditions, common Rayleigh damping, the retained phenomenological Kinematic material rule and idealised full bond. ZD is not claimed to be the actual or uniformly most demanding site class. The macro-model cannot reproduce discrete cracking, mortar-joint separation, post-peak localisation, cyclic masonry damage, stiffness/strength degradation, masonry hysteretic dissipation, interface debonding or progressive collapse. The 2 MPa value is a project-specific design-control target rather than a universal tensile capacity. Multi-record analysis, site-specific geotechnical and material investigation, and verification of bond, anchorage and long-term durability are required before implementation.

Author contributions A.K.: conceptualisation, methodology, software, validation, formal analysis, investigation, data curation, visualisation and writing—original draft. Z.T.: conceptualisation, methodology, supervision, project administration, validation and writing—review and editing. M.E.: methodology, software support, validation, formal analysis and writing—review and editing. M.Y.: investigation, data curation, visualisation, resources and writing—review and editing. A.E.S.: resources, investigation, validation and writing—review and editing. P.U.E.: resources, supervision support and writing—review and editing. All authors reviewed and approved the final manuscript.

Funding This study was supported by the Recep Tayyip Erdogan University Development Foundation (Grant No. 020260070170507).

Data availability The datasets used and/or analysed during the current study available from the corresponding author on reasonable request.

Code availability No custom or bespoke algorithm, software tool or computational pipeline was developed in this study.

Declarations

Competing interests The authors declare no competing interests.

Open Access This article is licensed under a Creative Commons Attribution-NonCommercial-NoDerivatives 4.0 International License, which permits any non-commercial use, sharing, distribution and reproduction in any medium or format, as long as you give appropriate credit to the original author(s) and the source, provide a link to the Creative Commons licence, and indicate if you modified the licensed material. You do not have permission under this licence to share adapted material derived from this article or parts of it. The images or other third party material in this article are included in the article's

Creative Commons licence, unless indicated otherwise in a credit line to the material. If material is not included in the article's Creative Commons licence and your intended use is not permitted by statutory regulation or exceeds the permitted use, you will need to obtain permission directly from the copyright holder. To view a copy of this licence, visit http://creativecommons.org/licenses/by-nc-nd/4.0/.

References

1. Aşıkoğlu, A., Avşar, Ö., Lourenço, P. B. & Silva, L. C. Effectiveness of Seismic Retrofitting of a Historical Masonry Structure: Kütahya Kurşunlu Mosque, Turkey. *Bull. Earthq. Eng.* **17**, 3365–3395. https://doi.org/10.1007/s10518-019-00603-6 (2019).
2. Şentürk, İ, Ergün, M. & Artar, M. Seismic Behavior Assessment of Historical Alaeddin Bey Mosque and Strengthening Suggestions by CFRP Fabric and Steel Plate. *Eng. Fail. Anal.* **137**, 106242. https://doi.org/10.1016/j.engfailanal.2022.106242 (2022).
3. Turk, A. M. & Cosgun, C. Seismic Behaviour and Retrofit of Historic Masonry Minaret. *Građevinar* **64**, 39–45. https://doi.org/10.14256/JCE.629.2011 (2012).
4. Usta, P. Assessment of Seismic Behavior of Historic Masonry Minarets in Antalya. *Turkey. Case Stud. Constr. Mater.* **15**, e00665. https://doi.org/10.1016/j.cscm.2021.e00665 (2021).
5. Demirtaş, B., Yanik, Y., Aymelek, A., Türker, T. & Yıldırım, Ö. Modal Testing and Full-Scale Seismic Evaluation of a Historical Minaret According to the 2023 Kahramanmaraş Earthquake and TBEC 2018 Design Spectrum. *Eng. Comput.* **42**, 1616–1640. https://doi.org/10.1108/EC-12-2024-1062 (2025).
6. Demirtaş, B., Türker, T., Yanik, Y. & Dede, T. Frequency-Based Damage Detection with ANN and Seismic Behaviour Assessment of a Historical Masonry Tower. *Iran. J. Sci. Technol. Trans. Civ. Eng.* **50**, 621–646. https://doi.org/10.1007/s40996-025-01816-3 (2026).
7. Hökelekli, E., Demir, A., Ercan, E., Nohutçu, H. & Karabulut, A. Seismic Assessment in a Historical Masonry Minaret by Linear and Non-Linear Seismic Analyses. *Period. Polytech. Civ. Eng.* **64**, 438–448. https://doi.org/10.3311/PPci.15126 (2020).
8. Işık, E. et al. Architectural Characteristics and Seismic Vulnerability Assessment of a Historical Masonry Minaret Under Different Seismic Risks and Probabilities of Exceedance. *Buildings* **12**, 1200. https://doi.org/10.3390/buildings12081200 (2022).
9. Artar, M. et al. Investigation on Seismic Isolation Retrofit of a Historical Masonry Structure. *Earthq. Struct.* **16**, 501–512. https://doi.org/10.12989/eas.2019.16.4.501 (2019).
10. Dogangun, A., Acar, R., Sezen, H. & Livaoglu, R. Investigation of Dynamic Response of Masonry Minaret Structures. *Bull. Earthq. Eng.* **6**, 505–517. https://doi.org/10.1007/s10518-008-9066-5 (2008).
11. Yanik, Y. et al. Investigation of Environmental Effects Through Long-Term Vibration Monitoring on the Structural Behavior and Seismic Performance Assessment of the Hagia Sophia Bell Tower. *Eng. Fail. Anal.* **182**, 110171. https://doi.org/10.1016/j.engfailanal.2025.110171 (2025).
12. Tonyali, Z. & Kiral, A. Evaluation of Earthquake-Related Damages on the Reinforced Concrete Buildings due to the February 6, 2023 Kahramanmaras-Turkiye Earthquakes. *Recep Tayyip Erdogan Univ. J. Sci. Eng.* **5**, 89–114. https://doi.org/10.53501/rteufemud.1471964 (2024).
13. Atmaca, B. Field Observations and Numerical Investigations on Seismic Damage Assessment of RC and Masonry Minarets During the February 6th, 2023, Kahramanmaraş (Mw 7.7 Pazarcık and Mw 7.6 Elbistan) Earthquakes in Türkiye. *Int. J. Archit. Herit.* **19**, 1117–1142. https://doi.org/10.1080/15583058.2024.2337651 (2025).
14. Gürbüz, A., Demirtaş, B. & Tonyali, Z. Seismic Performance Assessment of a Historical Masonry Mosque Minaret Under Pulse-Like and Non-Pulse-Like Near-Fault Ground Motions. *Buildings* **16**, 1108. https://doi.org/10.3390/buildings16061108 (2026).
15. Kocaman, I., Kazaz, I. & Kazaz, E. Seismic Load Capacity of Historical Masonry Mosques by Rigid Body Kinetics. *Int. J. Archit. Herit.* **14**, 849–869. https://doi.org/10.1080/15583058.2019.1570389 (2020).
16. Jadallah, M., Alghamri, R. & Doğangün, A. Seismic retrofitting of the historic Şirvani Mosque using fiber-reinforced polymer (FRP): A case study. *Eng. Fail. Anal.* **180**, 109898. https://doi.org/10.1016/j.engfailanal.2025.109898 (2025).
17. Jadallah, M., Almustafa, M. K., Doğangün, A. & Nehdi, M. L. Nonlinear Analysis of Historical Toptaş Minaret and FRP Strengthening for Sequence Earthquake Events. *J. Build. Pathol. Rehabil.* **10**, 57. https://doi.org/10.1007/s41024-025-00566-z (2025).
18. Almeida, F. P. A. & Cecchi, A. Mechanics of structure genome applied in the homogenization of masonry reinforced by FRP repointing technique. *Comput. Struct.* **253**, 106576. https://doi.org/10.1016/j.compstruc.2021.106576 (2021).
19. Alotaibi, K. S., Saiful Islam, A. B. M. & Galal, K. Axial Performance of Grouted C-Shaped Concrete Block Masonry Columns Jacketed by Carbon and Glass FRP. *Eng. Struct.* **267**, 114698. https://doi.org/10.1016/j.engstruct.2022.114698 (2022).

20. Alotaibi, K. S., AbdelRahman, B. & Galal, K. Analytical Study and Design Approach of the Axial and Flexural Response of Reinforced Masonry Columns Confined with FRP Jackets. *Eng. Struct.* **269**, 114805. https://doi.org/10.1016/j.engstruct.2022.114805 (2022).
21. Tarhan, İH. Stepwise FRP Strengthening of Historical Masonry Minarets: Nonlinear Seismic Assessment Based on a Minaret Collapsed During the 2023 Kahramanmaraş Earthquakes. *Eng. Fail. Anal.* **180**, 109933. https://doi.org/10.1016/j.engfailanal.2025.109933 (2025).
22. Yavartanoo, F., Kim, C. S., Bolhassani, D. & Kang, T. H. K. Macro-Modeling of CFRP Strengthening in U-Shaped Masonry Walls Under Combined Vertical and Out-of-Plane Loads. *Eng. Fail. Anal.* **177**, 109664. https://doi.org/10.1016/j.engfailanal.2025.109664 (2025).
23. Celik, T. Strengthening Strategies for Unreinforced Stone Masonry Walls Using FRP and CFM Composites. *Sci. Rep.* **15**, 28167. https://doi.org/10.1038/s41598-025-13747-0 (2025).
24. Mercimek, Ö. An experimental study about unreinforced masonry panels strengthening with CFRP: Out-of-plane failure. *Eng. Fail. Anal.* **181**, 109932. https://doi.org/10.1016/j.engfailanal.2025.109932 (2025).
25. Kiral, A., Tonyali, Z. & Elias, S. Optimizing Seismic Performance of Base-Isolated Buildings with Mass and Stiffness Variations Under Near and Far Fault Ground Motions. *Structures* **76**, 109026. https://doi.org/10.1016/j.istruc.2025.109026 (2025).
26. De Luca, A., Mele, E., Molina, J., Verzeletti, G. & Pinto, A. V. Base Isolation for Retrofitting Historic Buildings: Evaluation of Seismic Performance Through Experimental Investigation. *Earthq. Eng. Struct. Dyn.* **30**, 1125–1145. https://doi.org/10.1002/eqe.54 (2001).
27. Kiral, A., Ergün, M., Tonyali, Z., Artar, M. & Şentürk, İ. A Case Study Comparing Seismic Retrofitting Techniques for a Historically Significant Masonry Building's Minaret. *Eng. Fail. Anal.* **166**, 108873. https://doi.org/10.1016/j.engfailanal.2024.108873 (2024).
28. Habieb, A. B., Valente, M. & Milani, G. Hybrid seismic Base Isolation of a Historical Masonry Church Using Unbonded Fiber Reinforced Elastomeric Isolators and Shape Memory Alloy Wires. *Eng. Struct.* **196**, 109281. https://doi.org/10.1016/j.engstruct.2019.109281 (2019).
29. Habieb, A. B., Valente, M. & Milani, G. Base Seismic Isolation of a Historical Masonry Church Using Fiber Reinforced Elastomeric Isolators. *Soil Dyn. Earthq. Eng.* **120**, 127–145. https://doi.org/10.1016/j.soildyn.2019.01.022 (2019).
30. Losanno, D., Ravichandran, N., Parisi, F., Calabrese, A. & Serino, G. Seismic Performance of a Low-Cost Base Isolation System for Unreinforced Brick Masonry Buildings in Developing Countries. *Soil Dyn. Earthq. Eng.* **141**, 106501. https://doi.org/10.1016/j.soildyn.2020.106501 (2021).
31. Ergun, M., Tonyali, Z., Kiral, A. & Elias, S. Resilience-oriented seismic retrofit of heritage masonry minarets using hybrid base isolation and supplemental damping. *Structures* **83**, 110893. https://doi.org/10.1016/j.istruc.2025.110893 (2026).
32. Yiğit, M. E. Nonlinear Dynamic Analysis of earthquake Damage Reduction of Historical Minarets with Liquid Column Dampers. *Struct. Des. Tall Spec. Build.* **35**, e70123. https://doi.org/10.1002/tal.70123 (2026).
33. Kocaman, İ, Ertosun Yıldız, M., Yıldız, M. A., Eroğlu, E. & Çetin, S. A Proposal for Reinforcement of Historical Masonry Minarets: Gaziantep Kabasakal Mosque Minaret. *Buildings* **15**, 1213. https://doi.org/10.3390/buildings15081213 (2025).
34. Gulkan, P., Kazaz, İ & Kazaz, E. Diyarbakır Dört Ayaklı Minarenin Mw 7.7 ve 7.6 Kahramanmaraş depremleri sonrasındaki değerlendirmesi. *Turk. J. Civ. Eng.* **37**, 29–46. https://doi.org/10.18400/tjce.1732086 (2026).
35. Uğurlu, M. A., Erdemli Günaslan, S. & Karaşin, A. Dört Ayaklı Minare'nin modellenmesi ve yapısal analizi. *Dicle Univ. J. Eng.* **8**, 413–422 (2017). https://dergipark.org.tr/tr/pub/dumf/article/399629.
36. Usta Evci, P., Sever, A. E., Şakalak, E., Karimzadeh, S. & Lourenço, P. B. Seismic Damage Assessment of Minarets: Insights from the 6 February 2023 Kahramanmaraş earthquakes, Türkiye. *Buildings* **15**, 4358. https://doi.org/10.3390/buildings15234358 (2025).
37. Disaster and Emergency Management Presidency (AFAD). Turkish Accelerometric Database and Analysis System (TADAS): Earthquake map. https://tadas.afad.gov.tr/map (accessed 1 September 2026).
38. Öztürk, S. Earthquake Hazard Potential in the Eastern Anatolian Region of Turkey: Seismotectonic b and Dc-values and Precursory Quiescence Z-Value. *Front. Earth Sci.* **12**, 215–236. https://doi.org/10.1007/s11707-017-0642-3 (2018).
39. Kiral, A., Tonyali, Z. & Ergun, M. A Comprehensive Analysis of the Ground Motions of the 2023 Kahramanmaraş, Türkiye Earthquakes. *Earthq. Struct.* **28**, 203–219. https://doi.org/10.12989/eas.2025.28.3.203 (2025).
40. Republic of Türkiye, Disaster and Emergency Management Presidency (AFAD). Türkiye Building Earthquake Code (TBEC 2018). Official Gazette no. 30364 (18 March 2018). https://www.resmigazete.gov.tr/eskiler/2018/03/20180318M1-2.htm.
41. Ancheta, T. D. et al. NGA-West2 Database. *Earthq. Spectra* **30**, 989–1005. https://doi.org/10.1193/070913EQS197M (2014).
42. Seismosoft. SeismoMatch 2024: A Computer Program for Spectrum Matching of Earthquake Records. https://seismosoft.com/products/seismomatch/ (accessed 15 July 2026).
43. Al Atik, L. & Abrahamson, N. A. An Improved Method for Nonstationary Spectral Matching. *Earthq. Spectra* **26**, 601–617. https://doi.org/10.1193/1.3459159 (2010).

44. Karimzadeh, S. et al. Stochastic Simulation of Earthquake Ground Motions for the Seismic Assessment of Monumental Masonry Structures: Source-Based vs Site-Based Approaches. *Earthq. Eng. Struct. Dyn.* **53**, 303–330. https://doi.org/10.1002/eqe.4012 (2024).
45. Erçin Kahveci, A. & Kadayıfçı, A. Diyarbakır yöresi bazalt taşının yapısal özelliklerinin incelenmesi. *Int. J. Technol. Sci.* **5**, 56–69 (2013). https://dergipark.org.tr/tr/pub/utbd/article/273658.
46. Ministero delle Infrastrutture e dei Trasporti. Circolare 21 gennaio 2019, n. 7 C.S.LL.PP.: Istruzioni per l'applicazione dell'Aggiornamento delle Norme tecniche per le costruzioni. Gazzetta Ufficiale, Suppl. Ordinario no. 5 (2019).
47. Computers and Structures, Inc. SAP2000 v26: Integrated software for structural analysis and design. https://www.csiamerica.com/products/sap2000 (accessed 1 September 2026).
48. Lourenço, P. B. Computational strategies for masonry structures. Doctoral thesis, Delft University of Technology/University of Porto (1996).
49. Xu, R., Jin, Y. & Zhang, Y. Experimental Research on Brittleness and Rockburst Proneness of Three Kinds of Hard Rocks Under Uniaxial Compression. *Adv. Civ. Eng.* https://doi.org/10.1155/2021/8891633 (2021).
50. Computers and Structures, Inc. SAP2000 Help: Hysteresis types. https://docs.csiamerica.com/help-files/sap/Menus/Assign/Hysteresis_Types.htm (accessed 1 September 2026).
51. Computers and Structures, Inc. SAP2000 Help: Kinematic hysteresis model. https://docs.csiamerica.com/help-files/sap/Menus/Assign/Kinematic_Hysteresis_Model.htm (accessed 1 September 2026).
52. Pingaro, N., Buzzetti, M. & Milani, G. Advanced FE Nonlinear Numerical Modeling to Predict Historical Masonry Vaults Failure: Assessment of Risk Collapse for a Long Span Cloister Vault Heavily Loaded at the Crown by Means of a General-Purpose Numerical Protocol. *Eng. Fail. Anal.* **167**, 109070. https://doi.org/10.1016/j.engfailanal.2024.109070 (2025).
53. Caicedo, D. et al. Collapse Fragility Analysis of Historical Masonry Buildings Considering in-Plane and out-of-Plane Response of Masonry Walls. *Eng. Struct.* **319**, 118804. https://doi.org/10.1016/j.engstruct.2024.118804 (2024).
54. Zampieri, P., Zanini, M. A. & Modena, C. Simplified Seismic Assessment of Multi-Span Masonry Arch Bridges. *Bull. Earthq. Eng.* **13**, 2629–2646. https://doi.org/10.1007/s10518-015-9733-2 (2015).
55. Özmen, A. & Sayın, E. Seismic Assessment of a Historical Masonry Arch Bridge. *J. Struct. Eng. Appl. Mech.* **1**, 95–104. https://doi.org/10.31462/jseam.2018.01095104 (2018).
56. Özmen, A. & Sayın, E. Seismic Response of a Historical Masonry Bridge Under Near- and Far-Fault Ground Motions. *Period. Polytech. Civ. Eng.* **65**, 946–958. https://doi.org/10.3311/PPci.17832 (2021).
57. Canditone, C., Diana, L., Formisano, A., Rodrigues, H. & Vicente, R. Failure Mechanisms and Behaviour of Adobe Masonry Buildings: A Case Study. *Eng. Fail. Anal.* **150**, 107343. https://doi.org/10.1016/j.engfailanal.2023.107343 (2023).
58. Hoveidae, N., Fathi, A. & Karimzadeh, S. Seismic Damage Assessment of a Historic Masonry Building Under Simulated Scenario Earthquakes: A Case Study for Arge-Tabriz. *Soil Dyn. Earthq. Eng.* **147**, 106732. https://doi.org/10.1016/j.soildyn.2021.106732 (2021).
59. Benedetti, D., Carydis, P. & Pezzoli, P. Shaking Table Tests on 24 Simple Masonry Buildings. *Earthq. Eng. Struct. Dyn.* **27**, 67–90. https://doi.org/10.1002/(SICI)1096-9845(199801)27:1%3c67::AID-EQE719%3e3.0.CO;2-K (1998).
60. Formisano, A., Krstevska, L., Di Lorenzo, G., Landolfo, R. & Tashkov, L. Experimental Ambient Vibration Tests and Numerical Investigation on the Sidoni Palace in Castelnuovo of San Pio (L'Aquila, Italy). *Int. J. Masonry Res. Innov.* **3**, 269–294. https://doi.org/10.1504/IJMRI.2018.093487 (2018).
61. Kiral, A. & Tonyali, Z. The Effect of LRB Stiffness Changes With and Without Supplemental Viscous Dampers on Seismic Responses of an Experimentally Verified mdof Building. *Sigma J. Eng. Nat. Sci.* **43**, 301–315. https://doi.org/10.14744/sigma.2024.00104 (2025).
62. Yang, T. & Zhang, H. Seismic Safety Assessment of Base-Isolated Buildings Using Lead-Rubber Bearings. *Earthq. Spectra* **35**, 1087–1108. https://doi.org/10.1193/050318EQS108M (2019).
63. Jabbareh Asl, M., Rahman, M. M. & Karbakhsh, A. Numerical Analysis of Seismic Elastomeric Isolation Bearing in Base-Isolated Buildings. *Open J. Earthq. Res.* **3**, 1–4. https://doi.org/10.4236/ojer.2014.31001 (2014).
64. Arfen. Seismic Isolation Systems and Product Information. https://arfen.com.tr (accessed 15 July 2026).
65. Ergün, M. & Ateş, Ş. Evaluation of Dynamic and Fatigue Behaviour of Damaged Steel Beams Strengthened with Different Types of Techniques and a New Strengthening Method Proposal. *Arab. J. Sci. Eng.* **49**, 4969–4994. https://doi.org/10.1007/s13369-023-08233-6 (2024).
66. European Committee for Standardization (CEN). EN 10025-2:2004, Hot rolled products of structural steels—Part 2: Technical delivery conditions for non-alloy structural steels. CEN, Brussels (2004).
67. Republic of Türkiye, General Directorate of Foundations. Tarihi Yapılar İçin Deprem Risklerinin Yönetimi Kılavuzu [Earthquake Risk Management Guide for Historic Buildings]. General Directorate of Foundations, Ankara (2017). ISBN 978-975-19-6779-4.
68. Durgut, E., Ispir, M. & Ilki, A. Seismic Fragility Curves of a Historical Brick Masonry Minaret. *Earthq. Spectra* **41**, 3499–3525. https://doi.org/10.1177/87552930251342827 (2025).

Publisher's note Springer Nature remains neutral with regard to jurisdictional claims in published maps and institutional affiliations.

Authors and Affiliations

Adnan Kiral[1] · Zeliha Tonyali[1] · Mustafa Ergun[2] · Muhammet Yurdakul[3] · Ali Ekber Sever[4] · Pınar Usta Evci[4]

✉ Zeliha Tonyali
zeliha.tonyali@erdogan.edu.tr

[1] Department of Civil Engineering, Faculty of Engineering and Architecture, Recep Tayyip Erdogan University, 53100 Rize, Turkey

[2] Department of Civil Engineering, Faculty of Engineering, Bayburt University, 69010 Bayburt, Turkey

[3] Department of Civil Engineering, Faculty of Technology, Karadeniz Technical University, 61830 Trabzon, Turkey

[4] Department of Civil Engineering, Faculty of Technology, Isparta University of Applied Sciences, 32040 Isparta, Turkey